Radiogenic Sr-Nd-Pb isotope behavior in different grain-sized fine lithic materials during basalt weathering

Shivam Sahu[1], Satinder Pal Singh[1*], Kumar Batuk Joshi[2,3], and Yogita Kadlag[4]

[1]Department of Earth and Environmental Sciences, Indian Institute of Science Education and Research Bhopal, 462066, Madhya Pradesh, India

[2]Department of Geology, Central University of Himachal Pradesh, Dharamshala, Kangra, 176215, India

[3]National Centre for Earth Science Studies, Thiruvananthapuram, 695011, Kerala, India

[4]Geosciences Division, Physical Research Laboratory, Ahmedabad, 380009, Gujarat, India

[*]Corresponding author: Satinder Pal Singh (satinder@iiserb.ac.in)

Abstract

Radiogenic isotopes are widely used as sediment provenance tracers; however, their weathering response has not been fully established. This study investigates the weathering sensitivity of Sr-Nd-Pb isotopes in fine lithic fractions (FLF; grain size <2 μm, <5 μm, and <20 μm) capable of long-range transport. Geochemical and isotope compositions have been measured in the physicochemically separated FLF from soil (n = 5) and saprolite (n = 10) samples, along with the bedrock (n = 5) and dike (n = 1) outcrops, all belonging to a small basaltic watershed (~5 km^2) in the western Deccan Trap, India. The CIA (chemical index of alteration) varies from 75 to 97 (89 ± 13 (2 SD), n = 15) and 55 to 97 (84 ± 20, n = 30), while MIA(O) (mafic index of alteration under oxidizing condition) ranges from 64 to 86 (75 ± 14, n = 15) and 48 to 79 (64 ± 16, n = 30) in the soil FLF and saprolite FLF, respectively. The $^{87}Sr/^{86}Sr$ generally increases with grain-size reduction, while Nd and Pb isotopes show an insignificant grain-size effect. The bedrock normalized fractionation factors (α) of $^{87}Sr/^{86}Sr$, $^{143}Nd/^{144}Nd$, $^{206}Pb/^{204}Pb$, $^{207}Pb/^{204}Pb$, and $^{208}Pb/^{204}Pb$ obtained for the soil FLF (except those influenced by dike) are 1.015 ± 0.027 (n = 12), 1.0000 ± 0.0001 (n = 12), 1.031 ± 0.024 (n = 5), 1.008 ± 0.007 (n = 5), and 1.010 ± 0.008 (n = 5), while these factors for the saprolite FLF are 1.004 ± 0.007 (n = 30), 1.0000 ± 0.0001 (n = 29), 1.012 ± 0.008 (n = 14), 1.003 ± 0.002 (n = 14), and 1.004 ± 0.003 (n = 14), respectively. The average α values obtained for the saprolite FLF suggest insignificant fractionation of ~1 % for $^{87}Sr/^{86}Sr$ ($\Delta Sr/Al_2O_3$ –70 % to –98 %), ~1 unit ε_{Nd} ($\Delta Nd/Al_2O_3$ +46 % to –94 %), and ~1–2 % for Pb isotope ratios ($\Delta Pb/Al_2O_3$ +11 % to –84 %) during moderate to intense weathering of the Deccan Basalt. In contrast, the soil FLF samples show much higher α ranges for $^{87}Sr/^{86}Sr$ (up to 1.042 for $\Delta Sr/Al_2O_3$ –98 %) and $^{206}Pb/^{204}Pb$ (up to 1.045 for $\Delta Pb/Al_2O_3$ +52 %), but the α ranges for Nd isotopes are still similar to those of the saprolite FLF. The significant positive correlations of $^{87}Sr/^{86}Sr$ with CIA (R^2 = 0.43, $p < 0.01$), MIA(O) (R^2 = 0.51, $p < 0.01$) and MnO/Al_2O_3 (R^2 = 0.80, $p < 0.0001$) for the soil FLF reveals a preferential incorporation of ^{87}Sr from unknown source(s) into the residual Mn-oxides, which leads to the grain size-cum-weathering dependency of Sr isotopes. This study highlights the Nd and Pb isotope-based reliable provenance tracing of fine lithic materials; a maximum felsic dust contribution of <10 % to the soil FLF is quantified here. Meanwhile, the radiogenic Sr incorporation in secondary minerals poses a risk of overestimating the contributions from older granitic terranes using $^{87}Sr/^{86}Sr$-based mixing calculations.

Keywords: Tropical flood basalt; Deccan Basalt, Radiogenic isotopes; Weathering; Sediment provenance; Grain-size effect

1 Introduction

Radiogenic isotopes have been extensively used for sediment source apportionment, particularly over the Indian subcontinent (Amir et al., 2025; Bhattacharyya et al., 2024; Clift et al., 2002; Rahaman et al., 2009; Singh et al., 2017) and adjacent seas (Ahmad et al., 2005; Ali et al., 2015; Ehlert et al., 2011; Goswami et al., 2012; Karri et al., 2024; Li et al., 2018; Singh et al., 2023). Such studies rely on the basic assumption that the source rock-isotope signatures are well-preserved in soils and sediments undergoing sedimentary processes. Contrary to this assumption, significant Sr-Nd-Pb isotopic deviations from source rock compositions, as measured in soils, sediments, and leachates on a weathering profile-to-watershed scale, have also been frequently reported after the pioneering studies (Dasch, 1969; Erel et al., 1994; Goldstein and Jacobsen, 1987). These isotopic differences could partly be ascribed to eolian dust assimilation (Babechuk et al., 2015; Li et al., 2016; Mason et al., 2000; Sharma et al., 2025). Moreover, a significant radiogenic isotope fractionation is also feasible during differential mineral dissolution and/or incongruent weathering (i.e., preferential isotopic release from (or sorption onto) host minerals) under favorable hydroclimate and aging of developed soils (Blum and Erel, 1997; Dausmann et al., 2019; Dosseto et al., 2015; Erel et al., 1994; Harlavan et al., 1998; Horbe et al., 2022). For example, rapid weathering of biotite and plagioclase relative to K-feldspar from freshly exposed mineral surfaces may release radiogenic/unradiogenic Sr (Bayon et al., 2021; Blum and Erel, 1997). Whereas the preferential release of radiogenic Nd and Pb is generally linked to accessory heavy mineral weathering (Dausmann et al., 2019; Erel et al., 1994; Ma et al., 2010). These preferentially released isotopes, depending on their sorption onto or desorption from secondary minerals (e.g., Fe-Mn (oxy)hydroxides, carbonates, phosphates, etc.), may influence the particulate/solute isotopic budgets. In addition to weathering, heavy mineral/grain-size sorting and sediment contribution from diverse lithologies may also fractionate radiogenic Sr-Nd-Pb isotopes (Banerji et al., 2022; Bayon et al., 2021; Bayon et al., 2015; Garçon and Chauvel, 2014; Garçon et al., 2013, 2014; Jonell et al., 2018). Radiogenic isotope fractionation studies on monolithic weathering profiles are scarce (Babechuk et al., 2015; Ma et al., 2010). However, such studies are helpful in circumventing the sedimentary complexity posed by heterogeneous lithologies in large river basins and sorting during long-range transport.

The grain-size variability of radiogenic Sr, Nd, and/or Pb isotopes has generally been assessed in surface soils and fluvial/eolian sediments during their transit or postdeposition (Chen et al., 2007; Feng et al., 2010; Feng et al., 2009; Gili et al., 2016; Guinoiseau et al., 2022; Meyer et al., 2011; Pryor et al., 2025). In this context, the collective exploration of radiogenic Sr-Nd-Pb isotopes in fine lithic silicates of different grain-size fractions, produced by in situ weathering of a monolithic substrate, is currently lacking but crucial for their provenance tracing potential over long-range transport. This study examines the tropical flood basalt weathering response of Sr-Nd-Pb isotope systematics in fine lithic fractions (FLF) with grain sizes of <2 μm, <5 μm, and <20 μm. The weathering profiles were sampled from the Dhom Lake watershed, which is developed over the rapidly eroding western Deccan Trap in India (Fig. 1). The Deccan Trap is an extensive tropical flood basalt province and is vulnerable to rapid chemical weathering (Dessert et al., 2001; Widdowson and Cox, 1996). So it is considered a significant source of solutes and detrital sediment delivery to the northern Indian Ocean (Kessarkar et al., 2003; Kulkarni et al., 2024; Yu et al., 2019).

2 Study area

The Deccan Trap occupies an area of ~5 × 10^5 km^2 in peninsular India (Krishnamurthy, 2020). Approximately 90 % of this voluminous continental flood basalt was swiftly outpoured within 1 Ma (~66.5–65.5 Ma; Schoene et al., 2019). The Deccan stratigraphy is best exposed along the Western Ghat escarpment and consists of three successive lava flow subgroups (Kale and Pande, 2022): Kalsubai (66.413 ± 0.067 Ma to 66.105 ± 0.102 Ma), Lonavala (66.158 ± 0.082 Ma to 65.974 ± 0.084 Ma), and Wai (65.977 ± 0.151 Ma to 65.422 ± 0.013 Ma). The Kalsubai subgroup comprises the older lava formations of Jawhar, Igatpuri, Neral, Thakurwadi, and Bhimashankar. The relatively younger lava formations belong to the Lonavala (Bushe and Khandala) and the Wai (Poladpur, Ambenali, Mahabaleshwar, Panhala, and Desur) subgroups.

The post-lava emplacement warm-humid tropical climate has produced a thick red/black soil cover and laterites in western India (Widdowson and Gunnell, 1995). The low-lying areas of the Konkan Coastal Belt (KCB), particularly south of 18 °N, have red soils and well-preserved Tertiary laterites (Ollier and Sheth, 2008). The northern KCB region has the recent soil exposures and the basaltic bedrock outcrops due to a higher erosion rate, coupled with differential uplift in the Late Tertiary (Widdowson and Cox, 1996). The northern KCB presents an ideal sampling area for exploring radiogenic Sr-Nd-Pb isotope variations in fine lithic materials of soil and saprolite resulting from the weathering of tropical flood basalt.

Three weathering profiles of Dhom Lake catchment (area ~5 km^2 and elevation 80 m asl; Fig. 1c) in Raigad, Maharashtra, were selected for this study. The natural landscape lies within the core zone of the Indian Summer Monsoon (ISM) and receives an annual rainfall of ~3670 mm (CGWB, 2013). Despite warm and humid hydroclimate conditions (temperature ~17–32°C and relative humidity ~77 %; CGWB, 2013), favorable for the chemical weathering of the bedrock, weathering profiles of depth <10 m are generally exposed in the watershed owing to high erosion. A cross-cutting NNE–SSW–oriented dike, along with an earthen dam, is also located on the lake's western margin.

3 Materials and methods

3.1 Sampling

The physically distinctive soil/saprolite layers of three weathering profiles, namely P1 (n = 4), P3 (n = 5), and P5 (n = 6), along with a few outcrops of the bedrock (n = 5) and dike (n = 1), were collected during fieldwork in December 2019 (Fig. 1c). The profile P1 (depth 1.9 m and elevation 93 m asl) was developed on the steeply sloping eastern watershed of the lake. The profiles of P3 (depth 9.0 m and elevation 117 m asl) and P5 (depth 2.7 m and elevation 81 m asl) were developed on the gently sloping western watershed. The outcrop samples were broken with a geological hammer, while the weathering profiles were sampled after discarding 2–3 inches of aerial-exposed materials. The samples were stored in polyethylene ziplock packets and secured in cloth bags.

3.2 Sample preparation

The unweathered inner portions of the bedrock samples were pulverized using an agate ball-jar assembly (PM-100, Retsch). Additionally, large aliquots (~200 g) of the weathering profile samples were soaked for 48 hours in Milli-Q water (resistivity > 18.2 MΩ.cm) taken in 1000 mL polypropylene cylinders. The cylinders were intermittently subjected to ultrasonic treatment during the soaking process. These soaked samples were shaken well before differential gravitational settlings using

Stokes' law in the cleanroom at a temperature of ~22 °C. The top 10 cm supernatant, containing fine fractions of grain size <20 μm, <5 μm, and <2 μm, was siphoned off in 4.5 minutes, 73 minutes, and 7.5 hours, respectively (Gee and Or, 2002). The fine fractions were retrieved by centrifugation at 6000 rpm for 20 minutes. The fine lithic materials were obtained from the retrieved fractions by treatments with 5 % H_2O_2 and 0.5 N HBr to remove organic matter, carbonate, and Fe–Mn (oxy)hydroxides.

3.3 Elemental analysis

Aliquots (~0.1 g) of the pretreated grain-size segregated FLF from the weathering profiles, along with the pulverized dike sample, were acid-digested in the PFA vials (Savillex; capacity 7 ml) using high-purity HF-HCl-HNO_3 acids in the clean laboratory at IISER Bhopal following Qasim et al. (2022). The major and trace element concentrations were analyzed in the In-doped acid-digested sample solutions in 2 % HNO_3 using quadrupole ICP-MS (iCAP; ThermoFisher Scientific at IISER Bhopal) in the KED and STD mode, respectively. The external calibration curves were obtained using acid-digested BHVO-2 (dilution factors 2000, 5000, 7000, and 10000). The accuracy and precision of the elemental abundance measurements (~5–10%; Tables S1) were determined by analyzing BHVO-2 and duplicate unknown samples. The different analyte signals for total procedural blanks (n = 2) were found to be below detection levels (BDL).

3.4 Isotope analysis

Separate aliquots (~0.15 g) of the pulverized bedrock and fine lithic materials of weathering profiles were digested following the above analytical protocol. Pb, Sr, and Nd were purified from acid-digested sample solutions using sequential column chemistry following published protocols (Bhattacharyya et al., 2024; Lugmair and

Galer, 1992). Firstly, Pb was eluted from AG 1-X8 resin (BioRad, 200–400 mesh) using a mixture of 0.03 N HBr and 0.5 N HNO_3. In succession, Sr and Nd were eluted from the resins of AG 50W-X8 (BioRad, 200–400 mesh) and LN-B25-A (Triskem, 100–150 µm) using 2 N HCl and 0.16 N HCl, respectively. Radiogenic Pb isotope ratios ($^{206}Pb/^{204}Pb$, $^{207}Pb/^{204}Pb$, and $^{208}Pb/^{204}Pb$) were measured using the MC–ICPMS (Thermo Neptune XT) at IISc, Bangalore. The instrumental mass bias on Pb isotope ratios was corrected using the Tl-spiking technique (White et al., 2000). $^{206}Pb/^{204}Pb$, $^{207}Pb/^{204}Pb$, and $^{208}Pb/^{204}Pb$ obtained for the NIST SRM 981 (n = 11) were 16.937 ± 0.002 (2 SD), 15.491 ± 0.002, and 36.722 ± 0.005, respectively. The Sr-Nd isotope analysis was performed using MC-ICPMS (Nu-Plasma-3) at NCESS, Thiruvananthapuram. The Sr-Nd isotope compositions of a few samples (DB-23, DB-25, and BHVO-2) were analyzed using MC–ICPMS (Thermo Neptune Plus) at PRL Ahmedabad. The instrumental mass bias of $^{87}Sr/^{86}Sr$ and $^{143}Nd/^{144}Nd$ was corrected by normalizing $^{86}Sr/^{88}Sr$ and $^{146}Nd/^{144}Nd$ with 0.1194 and 0.7219, respectively. At NCESS, $^{87}Sr/^{86}Sr$ of 0.710234 ± 0.000016 was obtained for the NIST SRM 987 (n = 14), while $^{143}Nd/^{144}Nd$ of 0.512089 ± 0.000008 was found for JNdi-1 (n = 18), respectively. At PRL, $^{87}Sr/^{86}Sr$ of 0.710322 ± 0.000046 was obtained for the NIST SRM 987 (n = 40), while $^{143}Nd/^{144}Nd$ of 0.512109 ± 0.000015 was found for JNdi-1 (n = 20), respectively. The sample data are normalized to the reported value of $^{87}Sr/^{86}Sr$ (0.710248; Weis et al., 2006) for NIST SRM 987. The BHVO-2 duplicates (n = 2 for Sr-Nd and 4 for Pb isotopes) yield $^{87}Sr/^{86}Sr$ 0.703504 ± 0.000022, $^{143}Nd/^{144}Nd$ 0.512993 ± 0.000009, $^{206}Pb/^{204}Pb$ 18.628 ± 0.086, $^{207}Pb/^{204}Pb$ 15.537 ± 0.009, and $^{208}Pb/^{204}Pb$ 38.237 ± 0.053, agreeing well with the values reported by Weis et al. (2006). The analytical reproducibility (CV) of isotope measurements in duplicated unknown samples is $^{87}Sr/^{86}Sr$ 0.086 %, $^{143}Nd/^{144}Nd$ 0.006 %, $^{206}Pb/^{204}Pb$ 0.022 %, $^{207}Pb/^{204}Pb$

0.006 %, and $^{208}Pb/^{204}Pb$ 0.006 % (Table S2). The measured $^{143}Nd/^{144}Nd$ in samples is reported as the relative deviation (ε_{Nd} = $[^{143}Nd/^{144}Nd_{sample}/^{143}Nd/^{144}Nd_{CHUR}-1]\times10^4$) from the modern CHUR value (0.512638; Jacobsen and Wasserburg, 1980).

3.5 Grain-size analysis

Bulk materials of the weathering profiles were also analyzed for grain size distributions using a Laser-diffraction Particle Size Analyzer (Beckman Coulter LS™ 13 320) at BSIP, Lucknow. Before analysis, these samples were chemically treated with 10 % HCl and 30 % H_2O_2 to remove carbonate and organic matter, respectively (Vaasma, 2008). Subsequently, 1 % $Na_6(PO_3)_6$ was added to prevent grain flocculation. The mean grain size and sorting parameters were obtained following Folk and Ward (1957). The grain size distributions were further classified into sand (2000–63 μm), silt (2–63 μm), and clay (<2 μm) fractions.

4 Results

The geochemical and isotope compositions of different grain-sized FLF of soil and saprolite, and the bedrock/dike samples are presented in Tables 1 and 2. The grain size parameters obtained for the bulk materials of the weathering profiles (P1, P3, and P5) are provided in Table S3. The vertical distributions of the grain size parameters in these bulk materials are shown in Fig. 2. The mean grain size (M_z; Fig. 2a–c) shows a marked decrease upward in the profile P1 (~70–5 μm, average 25 μm). In contrast, no consistent M_z trend is seen in the profiles of P3 (~497–195 μm, average 378 μm) and P5 (~86–398 μm, average 254 μm) except for much lower M_z values in the topmost samples of P3-1 (~12 μm) and P5-1 (~5.4 μm). The sorting parameter (σ; Fig. 2d–f) ranges from ~1.1 to 2.7 (average 2.1) irrespective of the profiles, suggesting poorly to very poorly sorted materials primarily of the local origin. Further, the relative grain-size abundances (Fig. 2g–i) show that the silt is more abundant than sand in the bulk materials of the top three samples of P1 profile, along with the topmost samples of P3 and P5 profiles. For the sake of clarity, these silty samples (M_z <63 μm) are considered soil, while deeper sandy samples (M_z >63 μm) of the weathering profiles are classified as saprolite.

The Chemical Index of Alteration (CIA; McLennan, 1993; Nesbitt and Young, 1982) varies from 75 to 97 (89 ± 13, n = 15) and 55 to 97 (84 ± 20, n = 30) in the soil and the saprolite FLF, respectively. This incomplete kaolinization (CIA <100) suggests a progressive weathering scenario. Further, CIA in the size-segregated soil FLF ($CIA_{<2\ \mu m}$ 95 ± 4, $CIA_{<5\ \mu m}$ 91 ± 7, and $CIA_{<20\ \mu m}$ 82 ± 11) as well as saprolite FLF ($CIA_{<2\ \mu m}$ 89 ± 13, $CIA_{<5\ \mu m}$ 83 ± 18, and $CIA_{<20\ \mu m}$ 78 ± 24) suggests a grain size dependency of weathering intensity. The different grain-sized FLF of soil and saprolite in the ternary A–CN–K plot (Fig. 3a; Nesbitt and Young, 1984) generally exhibit moderate to intense plagioclase dissolution, while these FLF in the ternary A–L–F plot (Fig. 3b; Babechuk et al., 2014) show that the mafic mineral dissolution occurs to a moderate degree only. An oxic weathering environment is inferred from the ratio of the Mafic Index of Alteration in oxidizing to reducing conditions, MIA(O)/MIA(R) of 1.5 ± 0.2, following Babechuk et al. (2014).

Both the bedrock and dike materials are tholeiitic basalts as inferred from their major oxide abundances (Fig. S1; Jensen, 1976), but exhibit distinctly different radiogenic isotope compositions (Table 2). The $^{87}Sr/^{86}Sr$, ε_{Nd}, $^{206}Pb/^{204}Pb$, $^{207}Pb/^{204}Pb$, and $^{208}Pb/^{204}Pb$ of the bedrock (0.707 ± 0.001, –16.8 ± 3.1, 16.62 ± 0.16, 15.17 ± 0.03, and 37.22 ± 0.23) is better reflected by the saprolite FLF (0.710 ± 0.005, –15.5 ± 1.0, 16.82 ± 0.12, 15.22 ± 0.03, and 37.37 ± 0.11) rather than by the soil FLF (0.717 ±

0.018 (2 SD), –14.2 ± 5.1, 17.36 ± 0.94, 15.34 ± 0.19, and 37.79 ± 0.75). The unradiogenic ε_{Nd} of the basaltic bedrock itself is surprising and could result from crustal contamination during lava emplacement. On the other hand, the wider ranges of Sr-Nd-Pb isotope compositions obtained for the soil FLF than those of the saprolite FLF suggest multiple controls, including chemical weathering.

5 Discussion

5.1 Characterization of the bedrock and weathering profiles

Radiogenic Sr-Nd-Pb isotope compositions (Fig. 4a–d) of the bedrock and dike samples are distinctly different and contrasting from those of the Réunion plume signature (Nauret et al., 2019). The Réunion plume is generally considered a pristine mantle source of the Deccan magma. A plume-like isotopic signature has been reported earlier for the younger Wai subgroup of the western Deccan Trap, whereas the older lava formations of the Lonavala and Kalsubai subgroups exhibit crustal contamination (Basu et al., 2020; Peng et al., 1994). Previously, Peng et al. (1994) quantified substantial partial melting (up to 40 %) of the lower continental crust (LCC; Whitehouse, 1990) in these older lava formations. The bedrock samples of this study belong to the Kalsubai subgroup and are partly influenced by the LCC composition (Fig. 4a–d). In contrast, the dike sample lies in the overlapping fields of the Kalsubai and Lonavala subgroups. The lower ε_{Nd} values in the basaltic bedrock relative to the dike hint at a more pronounced lower crustal contamination during the initial stages of lava emplacement. Precisely, the bedrock samples are closer to the older lava formations of Neral and Thakurwadi, belonging to the Kalsubai subgroup. However, no outcrop of Neral (Salher) is found, but the Bhimashankar (Upper Ratangarh) and Thakurwadi (Lower Ratangarh) formations are exposed in the lake watershed (Fig. 1).

Thus, the bedrock samples are most likely of the Thakurwadi formation, which is also corroborated by their overlapping REE compositions (Sahu et al., 2025).

Figure 5 depicts the vertical distributions of Sr-Nd-Pb isotopes in the profile-wise soil/saprolite FLF. The radiogenic isotopes in the saprolite FLF better reflect the bedrock signature except for marginally higher $^{87}Sr/^{86}Sr$ in the deeper <2 μm samples of P3 and P5 profiles. A striking downward increasing trend of $^{87}Sr/^{86}Sr$ in the soil FLF of <2 μm and <5 μm in the P1 profile (Fig. 5a) probably suggests the downward migration of fine clays generally rich in radiogenic Sr (Dasch, 1969; Meyer et al., 2011). In contrast, Pb isotopes show upward increasing trends in this profile (Fig. 5c–e), which could be due to enhanced chemical weathering and/or extraneous input. The Nd and Pb isotope compositions of different grain-sized FLF of one exceptional soil sample (P3-1; Fig. 5g–j) are similar to the isotopically distinct dike composition.

5.2 Anthropogenic Pb input

The atmospheric Pb isotope composition exhibits systematic spatiotemporal variations in both the Northern and Southern Hemispheres (Bollhöfer and Rosman, 2000, 2001). Anthropogenic Pb sourced from leaded gasoline products, having Pb isotope ratios distinctly different from the felsic dust signatures, is known to be one of the major factors driving this spatiotemporal Pb isotope variability (Abouchami et al., 2013; Kumar et al., 2014; Kumar et al., 2018). Recent studies (Kumar et al., 2014; Rahaman et al., 2024; Sen et al., 2016; Yadav et al., 2025) have suggested that the atmospheric deposition of anthropogenic Pb, post-ban on the leaded gasoline usage, is still sourced from vehicular emissions along with the contributions from coal-powered thermal plants, waste incineration, ore smelting/refining, and other industrial activities.

In this study, anthropogenic Pb is chemically removed before the sample preparation for Pb isotope measurements (Guinoiseau et al., 2022). The anthropogenic Pb removal efficiency is reflected by Pb isotope compositions of the soil/saprolite FLF (except for those of P3-1 close to the dike) falling well outside the anthropogenic Pb envelopes of the global as well as Indian origins (Fig. 6). Further, the regression lines of the soil/saprolite FLF exhibit a more gentle slope than that of the proximal anthropogenic Pb sources of the Indian origin. Thus, a significant role of anthropogenic Pb in modifying the natural Pb isotope composition of the FLF is ruled out here.

5.3 Grain-size impact on radiogenic isotopes

Earlier studies (Chen et al., 2007; Feng et al., 2009; Meyer et al., 2011; Pryor et al., 2025) have documented insignificant ε_{Nd} (±1 unit) variations but significant increases of $^{87}Sr/^{86}Sr$ with grain size reduction in fine-to-coarse fluvial and eolian sediments. Whereas, significant but inconsistent Pb isotope variations with grain size reduction have been generally reported from natural deserts and sediment depocenters (Feng et al., 2010; Gili et al., 2016; Grousset and Biscaye, 2005; Guinoiseau et al., 2022). In this study, Sr isotopes are found to become more radiogenic with the grain size reduction, as shown in Fig. 7a–c. Meanwhile, the Nd and Pb isotope compositions of different grain-sized FLF fall on the 1:1 line in Fig. 7d–i. An enhanced degree of this Sr isotope decoupling from Nd and Pb isotopes is seen in the soil FLF as compared to that in the saprolite FLF. The grain-size dependency of radiogenic Sr isotopes in the soil FLF could result from weathering-induced fractionation (Dasch, 1969; Dou et al., 2025; Luo et al., 2024; Ma et al., 2010; Pryor et al., 2025) or variable provenance (Babechuk et al., 2015; Garçon and Chauvel, 2014; Li et al., 2016; Mason et al., 2000), as discussed in the following section.

5.4 Weathering impacts on radiogenic isotopes

The scatter plots of CIA (Fig. 8a–e) and MIA(O) (Fig. 8f–j) versus radiogenic Sr-Nd-Pb isotopes provide insights into the weathering controls on the isotopic variability of the soil/saprolite FLF. The $^{87}Sr/^{86}Sr$ in the soil FLF gradually exceeds the bedrock/dike composition, along with the elevated but constant values in the saprolite FLF of <2 µm only, at CIA >75 and MIA(O) >60 (Fig. 8a and f). The gradual $^{87}Sr/^{86}Sr$ variations in the soil FLF show significant but moderate correlations with CIA (R^2 = 0.43, p <0.01) and MIA(O) (R^2 = 0.51, p <0.01), despite the preferential plagioclase dissolution over mafic minerals. Recently, Sahu et al. (2025) identified abundant plagioclase and pyroxene minerals in the bedrock outcrops and pyroxene remnants in surface soils and aquatic sediments in this watershed. On the other hand, Pb and Nd isotopes in the soil/saprolite FLF generally overlap with the bedrock composition over the entire ranges of CIA (Fig. 8b–e) and MIA(O) (Fig. 8g–j). Anomalously elevated Nd and Pb isotope compositions found in the P3-1 and P1-1 soil FLF could be a dike/dust influence. Therefore, a progressive weathering influence on Sr isotopes is obvious; however, the weathering intensity alone seems insufficient in explaining the isotopic variations.

Further, the scatter plots (Fig. 9a–i) of Sr/Al_2O_3, Nd/Al_2O_3, Pb/Al_2O_3, MnO/Al_2O_3, and Th/Al_2O_3 versus radiogenic Sr-Nd-Pb isotopes are used to delineate the leaching/sorption influence and the UCC-like felsic dust input. The $^{87}Sr/^{86}Sr$ in the soil FLF substantially increases at low Sr/Al_2O_3 of $<4\times10^{-4}$ corresponding to a Sr removal of >90 % relative to the bedrock composition (Fig. 9a). Also, a strong positive correlation of MnO/Al_2O_3–$^{87}Sr/^{86}Sr$ (R^2 = 0.80, p <0.0001; Fig. 9b) is found in the soil FLF, indicating the capture of radiogenic Sr into residual oxides (leftover Fe-Mn coatings). This result contradicts the general hypothesis that unradiogenic Sr loss due to preferential plagioclase dissolution contributes to an increase of $^{87}Sr/^{86}Sr$ in silicate residues during progressive weathering (Bain and Bacon, 1994). Recently, Su et al. (2022) demonstrated the incorporation of lighter Sr isotopes (^{86}Sr) into secondary clays formed during the progressive weathering of granodiorite. The above MnO/Al_2O_3–$^{87}Sr/^{86}Sr$ correlation in the soil FLF, along with the elevated $^{87}Sr/^{86}Sr$ in the saprolite FLF (<2 μm) coupled with MnO removal of >60 %, does not lend support to the preferential ^{86}Sr release and incorporation into residual oxides/secondary clays of the analyzed FLF in this study. Rather, an isotopic exchange between these secondary minerals of FLF and an unknown dissolved pool of highly radiogenic Sr could lead to elevated $^{87}Sr/^{86}Sr$ in the soil/saprolite FLF, as reported elsewhere (Innocent et al., 1997). The rapid weathering of biotite over plagioclase is generally associated with the preferential release and likely capture of radiogenic Sr during the early stages of granitoid weathering (Blum and Erel, 1997). Although traces of biotite in the Deccan and Rajmahal Trap Basalts were reported previously (Baksi, 1995; Melluso and Sethna, 2011), any micaceous mineral (including biotite) could not be traced in the bedrock of this basaltic watershed (Sahu et al., 2025). A negligible role of felsic dust in contributing radiogenic pool Sr to the soil FLF is reflected by a poor correlation of Th/Al_2O_3–$^{87}Sr/^{86}Sr$ ($R^2 = 0.20$, $p < 0.1$; not shown in Fig. 9c). The lack of local rainwater Sr isotope data prevents us from firmly ruling out an extraneous source of radiogenic Sr (Innocent et al., 1997; Ma et al., 2010). However, the upper bound of $^{87}Sr/^{86}Sr$ in the soil FLF (~0.736) is much higher than that of the UCC composition (~0.716; Goldstein and Jacobsen, 1987) and the rainwater of Ahmedabad near the Thar Desert (~0.70878–0.71027; Chatterjee and Singh, 2012), suggesting a low likelihood of eolian input as a major unknown source of radiogenic Sr. Thus, the sorption of radiogenic Sr from unknown source(s) onto fine lithics during progressive weathering of Deccan Basalt is highlighted.

Moreover, Nd isotopes generally show insignificant variations (within ±1 ε_{Nd} unit; Fig. 9d) in the soil/saprolite FLF despite a Nd removal (up to 94 %) or addition (up to 78 %). The dike influence on the P3-1 soil FLF is clearly reflected by the scatter plots (Fig. 9d, f, g, and i) of Nd/Al_2O_3, Pb/Al_2O_3, and Th/Al_2O_3 versus Nd-Pb isotopes. A few soil FLF (P1-1 and P1-2) also show elevated $^{206}Pb/^{204}Pb$, Pb/Al_2O_3, MnO/Al_2O_3, and Th/Al_2O_3 relative to the bedrock composition (Fig. 9g–i). These elemental/isotopic ratios are increasing toward the UCC composition (McLennan, 2001; Millot et al., 2004), which indicates a minor felsic dust component in these samples. Limited studies (Babechuk et al., 2015; Mason et al., 2000) have also reported eolian dust-driven Sr and Nd isotopic variability in the intensely weathered lateritic profiles of Deccan Basalt.

The bedrock normalized Sr-Nd-Pb isotope fractionation factors (α) are calculated for the soil/saprolite FLF (Fig. 9 and Table S4). The α values are close to 1 for the saprolite FLF, while these values extend far from 1 for some of the soil FLF, additionally influenced by the dike/dust composition and radiogenic Sr-sorption (Figs. 9 and 10). Moreover, the probability distributions of the α values obtained for the soil/saprolite FLF are compared with those of the literature data (Fig. 10). The dike influence results in the bimodal probability distributions of α for Nd and Pb isotopes in the soil FLF (Fig. 10b–e). The literature data have been considered from typical weathering profiles developed on the basaltic (Bidar, Dalahi, Pakuria, Chengmai, and Hainan laterites; Babechuk et al., 2015; Luo et al., 2024; Ma et al., 2010; Sharma et al., 2025) and granitic (Sierra Nevada, Wind River Mountain, and Vosges Mountain profiles; Aubert et al., 2001; Blum and Erel, 1997; Harlavan et al., 1998) substrates.

The probability distribution of $\alpha_{87Sr/86Sr}$ for the soil/saprolite FLF is wider than that of the basaltic Hainan and Chengmai laterites, but narrower than that of the granitic Wind River Mountain and Vosges Mountains profiles (Fig. 10a). This result indicates that Sr isotopes fractionate to a large extent of –10 % to +4 % during progressive weathering. The relatively low $\alpha_{87Sr/86Sr}$ for the laterites could be attributed to the high aqueous mobility of Sr (Nesbitt et al., 1980), which leads to efficient Sr removal from primary as well as secondary minerals during extreme weathering of lateritization. Conversely, the weathering-induced isotope fractionation remains a topic of debate for particle-reactive Nd and Pb (Babechuk et al., 2015; Ma et al., 2010; Öhlander et al., 2000). Nd isotope fractionation at extreme weathering is reflected by $\alpha_{143Nd/144Nd}$ much lower than 1 in the lateritic profiles developed over the Deccan and Rajmahal Traps and the volcanic Island of Hainan (Fig. 10b). Whereas the α peaks for Nd and Pb isotopes are close to 1 in the case of the basaltic saprolite FLF and the granitic Sierra Nevada and Vosges Mountain profiles, suggesting little or insignificant isotope fractionation of Nd (±1 ε_{Nd}) and Pb (±1–2 %) during progressive weathering, irrespective of the lithology.

5.5 Implications for the provenance of fine lithic materials

Radiogenic Sr-Nd isotopes have been widely used for the provenance tracing of atmospheric dust (Aswini et al., 2022; Bikkina et al., 2023; Karri et al., 2024; Singh et al., 2023; Suresh et al., 2021), riverine floodplain/desert sediment (Amir et al., 2023; Amir et al., 2025; Awasthi et al., 2018; Bhattacharyya et al., 2024; Garzanti et al., 2020; George et al., 2024; Rahaman et al., 2009; Singh et al., 2008), and coastal as well as marine sediment (Ahmad et al., 2005; Carter et al., 2020; Clift et al., 2008; Colin et al., 1999; Goswami et al., 2012; Kessarkar et al., 2003; Li et al., 2018; Peketi et al., 2021). Whereas radiogenic Pb isotopes have been sparsely used for dust/sediment provenance in the region (Ali et al., 2015; Alizai et al., 2011; Garçon and Chauvel, 2014).

Previously, Babechuk et al. (2015) estimated that the felsic dust supply to the bulk materials of the Bidar lateritic profile in the Deccan Trap is up to 57 % based on the Nd isotope budget. The novel and literature datasets help quantify the eolian dust input to the fine sediments analyzed in this case study. The Pb and Nd isotope compositions of the soil/saprolite FLF (except those of P1-1 and P3-1 samples) generally fall close to the bedrock composition (Fig. 7a–d), suggesting their cogenetic relationship. Considering the binary endmember mixing lines in the Pb–Nd isotope space (Fig. 7d), the different grain-sized FLF of the P3-1 sample show ~70 % contribution of the dike-like materials, while those of P1-1 FLF lying far away from the bedrock and dike compositions show a maximum dust contribution of <10 % from the UCC-like felsic lithologies (Goldstein and Jacobsen, 1987; McLennan, 2001; Millot et al., 2004).

The Thar Desert, Indo-Gangetic Plain (IGP), and the Peninsular Gneissic Complexes (PGC, comprising major lithologies of Southern Granulites, Dharwar craton, Closepet granite, and Cuddapah basin; Shukla et al., 2024) are the potential felsic dust sources in the region. Here, the Thar dust signatures are retrieved from the extensive geochemical and Sr-Nd isotope dataset (Bhattacharyya et al., 2024) and the limited Pb isotope dataset (Ferrat et al., 2012) of the Thar sediments. For the IGP dust signatures, the Sr-Nd isotope dataset (Singh et al., 2008) and the Pb isotope dataset (Garçon and Chauvel, 2014) of the Himalayan foreland river sediments are considered. Shukla et al. (2024, and references therein) have compiled the Sr-Nd isotope signature of PGC. However, the Pb isotope signature of PGC was retrieved from the limited GEOROC dataset of Dharwar craton only (Digis, 2024).

The scatter plot of $^{206}Pb/^{204}Pb$–$^{207}Pb/^{204}Pb$ (Fig. 7a) shows that the regression lines of soil/saprolite FLF samples contrast with those of the IGP and PGC endmembers, while the limited dataset of Thar is distinguishable from these regression lines, which reveals a negligible felsic dust contribution. The felsic dust contribution of <10 % only to the soil/saprolite FLF is quantified based on the binary mixing lines of the bedrock with the Thar, IGP, and PGC endmembers in the Pb–Pb and Pb–Nd isotope spaces (Fig. 7a–d). The soil FLF (<2 μm and <5 μm) and the saprolite FLF (<2 μm) samples clearly deviate from the binary mixing lines with the Thar, IGP, or PGC endmembers in the Sr–Pb and Sr–Nd isotope spaces (Fig. 7e–f). This extraordinary Sr isotope trend, extending beyond the Thar and PGC compositions, leads to erroneous provenance results, implying a maximum felsic dust contribution of upto 84 % to the soil FLF from the IGP endmember using $^{87}Sr/^{86}Sr$-based mixing calculations. The elevated $^{87}Sr/^{86}Sr$, along with nearly constant Nd and Pb isotope compositions in different grain size FLF of each soil sample, is due to radiogenic Sr sorption onto secondary minerals formed during progressive weathering. Ignoring this radiogenic Sr sorption effect, even traces of secondary minerals in fine sediments could bias Sr isotope-based provenance toward older granitic terranes. Thus, radiogenic Nd-Pb isotopes are reliable provenance tracers, while Sr isotopes should be used with caution.

6 Conclusions

The weathering sensitivity of radiogenic Sr-Nd-Pb isotopes has been investigated in the FLF of the basaltic soils and saprolites developed in the western Deccan Trap. The Pb and Nd isotopes are found to be least affected by grain size effects in comparison to Sr isotopes and reflect the well-preserved bedrock signature during moderate to intense chemical weathering. The grain size variability of Sr isotopes is attributed to the sorption of more radiogenic Sr from unknown source(s) onto residual oxides in the fine lithics. Thus, radiogenic Pb and Nd isotopes are reliable provenance tracers of fine lithic sediments, while Sr isotopes should be used with caution.

Acknowledgments:

The authors thankfully acknowledge the Ministry of Earth Sciences, India, for providing financial support (MoES/P.O.(Geo)/168/2017) to S.P. Singh. Pritam Nasipuri from the EES Department at IISER Bhopal is thanked for sharing aliquots of USGS reference materials. The authors acknowledge the analytical support from IISER Bhopal (Ministry of Education), IISc Bangalore (Ministry of Education), BSIP Lucknow (Department of Science and Technology), NCESS Thiruvananthapuram (Ministry of Earth Sciences), and PRL Ahmedabad (Department of Space), Government of India.

Data availability: The novel dataset presented in this manuscript is available on the Mendeley Database (https://data.mendeley.com/datasets/kddgxj8j24/1).

References

Abouchami, W., Näthe, K., Kumar, A., Galer, S.J.G., Jochum, K.P., Williams, E., Horbe, A.M.C., Rosa, J.W.C., Balsam, W., Adams, D., Mezger, K. and Andreae, M.O. (2013) Geochemical and isotopic characterization of the Bodélé Depression dust source and implications for transatlantic dust transport to the Amazon Basin. Earth Planet. Sci. Lett. 380, 112-123.

Ahmad, S.M., Anil Babu, G., Padmakumari, V.M., Dayal, A.M., Sukhija, B.S. and Nagabhushanam, P. (2005) Sr, Nd isotopic evidence of terrigenous flux variations in the Bay of Bengal: Implications of monsoons during the last ~34,000 years. Geophys. Res. Lett. 32, L22711.

Ali, S., Hathorne, E.C., Frank, M., Gebregiorgis, D., Stattegger, K., Stumpf, R., Kutterolf, S., Johnson, J.E. and Giosan, L. (2015) South Asian monsoon history over the past 60 kyr recorded by radiogenic isotopes and clay mineral assemblages in the Andaman Sea. Geochemistry, Geophysics, Geosystems 16, 505-521.

Alizai, A., Clift, P.D., Giosan, L., VanLaningham, S., Hinton, R., Tabrez, A.R. and Danish, M. (2011) Pb isotopic variability in the modern-Pleistocene Indus River system measured by ion microprobe in detrital K-feldspar grains. Geochim. Cosmochim. Acta 75, 4771-4795.

Amir, M., Paul, D., Anchana, P., Tarique, M. and Rahaman, W. (2023) Geochemical evidence for west-flowing paleo-Yamuna River in northwest India during the late Quaternary and its implication for the Harappan Civilization. Geochemistry, 126021.

Amir, M., Paul, D., Yang, S. and Chang, Y.-P. (2025) Climate-controlled distribution of erosion over the Himalaya in the late Quaternary: Evidence from Sr-Nd isotope variability in paleo-Yamuna channel sediments. Quat. Sci. Rev. 351, 109179.

Aswini, M.A., Tiwari, S., Singh, U., Kurian, S., Patel, A., Gunthe, S.S. and Kumar, A. (2022) Aeolian Dust and Sea Salt in Marine Aerosols over the Arabian Sea during the Southwest Monsoon: Sources and Spatial Variability. ACS Earth and Space Chemistry 6, 1044-1058.

Aubert, D., Stille, P. and Probst, A. (2001) REE fractionation during granite weathering and removal by waters and suspended loads: Sr and Nd isotopic evidence. Geochimica et Cosmochimica Acta 65, 387-406.

Awasthi, N., Ray, E. and Paul, D. (2018) Sr and Nd isotope compositions of alluvial sediments from the Ganga Basin and their use as potential proxies for source identification and apportionment. Chem. Geol. 476, 327-339.

Babechuk, M.G., Widdowson, M. and Kamber, B.S. (2014) Quantifying chemical weathering intensity and trace element release from two contrasting basalt profiles, Deccan Traps, India. Chemical Geology 363, 56-75.

Babechuk, M.G., Widdowson, M., Murphy, M. and Kamber, B.S. (2015) A combined Y/Ho, high field strength element (HFSE) and Nd isotope perspective on basalt weathering, Deccan Traps, India. Chem. Geol. 396, 25-41.

Bain, D.C. and Bacon, J.R. (1994) Strontium isotopes as indicators of mineral weathering in catchments. Catena 22, 201-214.

Baksi, A.K. (1995) Petrogenesis and timing of volcanism in the Rajmahal flood basalt province, northeastern India. Chem. Geol. 121, 73-90.

Banerji, U.S., Dubey, C.P., Goswami, V. and Joshi, K.B. (2022) Geochemical Indicators in Provenance Estimation, in: Armstrong-Altrin, J.S., Pandarinath, K., Verma, S.K. (Eds.), Geochemical Treasures and Petrogenetic Processes. Springer Nature Singapore, Singapore, pp. 95-121.

Basu, A.R., Saha-Yannopoulos, A. and Chakrabarty, P. (2020) A precise geochemical volcano-stratigraphy of the Deccan traps. Lithos 376-377, 105754.

Bayon, G., Freslon, N., Germain, Y., Bindeman, I.N., Trinquier, A. and Barrat, J.-A. (2021) A global survey of radiogenic strontium isotopes in river sediments. Chemical Geology 559, 119958.

Bayon, G., Toucanne, S., Skonieczny, C., André, L., Bermell, S., Cheron, S., Dennielou, B., Etoubleau, J., Freslon, N., Gauchery, T., Germain, Y., Jorry, S.J., Ménot, G., Monin, L., Ponzevera, E., Rouget, M.L., Tachikawa, K. and Barrat, J.A. (2015) Rare earth elements and neodymium isotopes in world river sediments revisited. Geochimica et Cosmochimica Acta 170, 17-38.

Bhattacharyya, R., Singh, S.P., Qasim, A. and Chandrashekhar, A.K. (2024) Geochemical and Radiogenic Sr-Nd Isotope Characterization of Widespread Sandy Surface Sediments in the Great Indian Desert, Thar: Implications for Provenance Studies. Journal of Geophysical Research: Earth Surface 129, e2023JF007625.

Bikkina, S., Shukla, A., Singh, S.K., Karri, D., Singh, N.D. and Sahoo, B. (2023) Link of the short-term temporal trends of Sr and Nd isotopic composition of aeolian dust over the Arabian Sea with the source emissions. Sci. Tot. Environ. 892, 164680.

Blum, J.D. and Erel, Y. (1997) Rb-Sr isotope systematics of a granitic soil chronosequence: The importance of biotite weathering. Geochim. Cosmochim. Acta 61, 3193-3204.

Bollhöfer, A. and Rosman, K.J.R. (2000) Isotopic source signatures for atmospheric lead: the Southern Hemisphere. Geochimica et Cosmochimica Acta 64, 3251-3262.

Bollhöfer, A. and Rosman, K.J.R. (2001) Isotopic source signatures for atmospheric lead: the Northern Hemisphere. Geochimica et Cosmochimica Acta 65, 1727-1740.

Carter, S.C., Griffith, E.M., Clift, P.D., Scher, H.D. and Dellapenna, T.M. (2020) Clay-fraction strontium and neodymium isotopes in the Indus Fan: implications for sediment transport and provenance. Geol. Mag. 157, 879-894.

CGWB (2013) Ground Water Information, Raigarh District, Maharashtra. Central Ground Water Board, https://cgwb.gov.in/sites/default/files/2022-10/raigarh_0.pdf

Chatterjee, J. and Singh, S.K. (2012) $^{87}Sr/^{86}Sr$ and major ion composition of rainwater of Ahmedabad, India: Sources of base cations. Atmos. Environ. 63, 60-67.

Chen, J., Li, G., Yang, J., Rao, W., Lu, H., Balsam, W., Sun, Y. and Ji, J. (2007) Nd and Sr isotopic characteristics of Chinese deserts: Implications for the provenances of Asian dust. Geochimica et Cosmochimica Acta 71, 3904-3914.

Clift, P.D., Giosan, L., Blusztajn, J., Campbell, I.H., Allen, C., Pringle, M., Tabrez, A.R., Danish, M., Rabbani, M.M., Alizai, A., Carter, A. and Luckge, A. (2008) Holocene erosion of the Lesser Himalaya triggered by intensified summer monsoon. Geology 36, 79-82.

Clift, P.D., Lee, J.I., Hildebrand, P., Shimizu, N., Layne, G.D., Blusztajn, J., Blum, J.D., Garzanti, E. and Khan, A.A. (2002) Nd and Pb isotope variability in the Indus River System: implications for sediment provenance and crustal heterogeneity in the Western Himalaya. Earth Planet. Sci. Lett. 200, 91-106.

Colin, C., Turpin, L., Bertaux, J., Desprairies, A. and Kissel, C. (1999) Erosional history of the Himalayan and Burman ranges during the last two glacial-interglacial cycles. Earth Planet. Sci. Lett. 171, 647-660.

Das, R., Bin Mohamed Mohtar, A.T., Rakshit, D., Shome, D. and Wang, X. (2018) Sources of atmospheric lead (Pb) in and around an Indian megacity. Atmospheric Environment 193, 57-65.

Dasch, E.J. (1969) Strontium isotopes in weathering profiles, deep-sea sediments, and sedimentary rocks. Geochimica et Cosmochimica Acta 33, 1521-1552.

Dausmann, V., Gutjahr, M., Frank, M., Kouzmanov, K. and Schaltegger, U. (2019) Experimental evidence for mineral-controlled release of radiogenic Nd, Hf and Pb isotopes from granitic rocks during progressive chemical weathering. Chemical Geology 507, 64-84.

Dessert, C., Dupré, B., François, L.M., Schott, J., Gaillardet, J., Chakrapani, G. and Bajpai, S. (2001) Erosion of Deccan Traps determined by river geochemistry: impact on the global climate and the 87Sr/86Sr ratio of seawater. Earth Planet. Sci. Lett. 188, 459-474.

Digis, T. (2024) 2024-12-1KRR1P_Dharwar_Craton_Archean.csv, GEOROC Compilation: Archaean Cratons, V10 ed. GRO.data.

Dosseto, A., Vigier, N., Joannes-Boyau, R.C., Moffat, I., Singh, T. and Srivastava, P. (2015) Rapid response of silicate weathering rates to climate change in the Himalaya. Geochemical Perspectives Letters V1, 10-19.

Dou, R., Zou, J., Shi, X., Dong, Z., Wu, Y., Zhu, A., Feng, X., Zou, X., Gorbarenko, S., Vasilenko, Y. and Bosin, A. (2025) Contrasting Mechanisms Controlling Pb Isotopes of Dust in Inland and Marine Archives. Geophys. Res. Lett. 52, e2024GL114133.

Ehlert, C., Frank, M., Haley, B.A., Böniger, U., De Deckker, P. and Gingele, F.X. (2011) Current transport versus continental inputs in the eastern Indian Ocean: Radiogenic isotope signatures of clay size sediments. Geochem. Geophys. Geosyst. 12, Q06017.

Erel, Y., Harlavan, Y. and Blum, J.D. (1994) Lead isotope systematics of granitoid weathering. Geochimica et Cosmochimica Acta 58, 5299-5306.

Feng, J.-L., Hu, Z.-G., Cui, J.-Y. and Zhu, L.-P. (2010) Distributions of lead isotopes with grain size in aeolian deposits. Terra Nova 22, 257-263.

Feng, J.-L., Zhu, L.-P., Zhen, X.-L. and Hu, Z.-G. (2009) Grain size effect on Sr and Nd isotopic compositions in eolian dust: Implications for tracing dust provenance and Nd model age. Geochem. J. 43, 123-131.

Ferrat, M., Weiss, D.J., Dong, S., Large, D.J., Spiro, B., Sun, Y. and Gallagher, K. (2012) Lead atmospheric deposition rates and isotopic trends in Asian dust during the last 9.5kyr recorded in an ombrotrophic peat bog on the eastern Qinghai–Tibetan Plateau. Geochimica et Cosmochimica Acta 82, 4-22.

Folk, R.L. and Ward, W.C. (1957) Brazos River bar [Texas]; a study in the significance of grain size parameters. Journal of Sedimentary Research 27, 3-26.

Garçon, M. and Chauvel, C. (2014) Where is basalt in river sediments, and why does it matter? Earth and Planetary Science Letters 407, 61-69.

Garçon, M., Chauvel, C., France-Lanord, C., Limonta, M. and Garzanti, E. (2013) Removing the "heavy mineral effect" to obtain a new Pb isotopic value for the upper crust. Geochemistry, Geophysics, Geosystems 14, 3324-3333.

Garçon, M., Chauvel, C., France-Lanord, C., Limonta, M. and Garzanti, E. (2014) Which minerals control the Nd–Hf–Sr–Pb isotopic compositions of river sediments? Chemical Geology 364, 42-55.

Garzanti, E., Liang, W., Andò, S., Clift, P.D., Resentini, A., Vermeesch, P. and Vezzoli, G. (2020) Provenance of Thal Desert sand: Focused erosion in the

western Himalayan syntaxis and foreland-basin deposition driven by latest Quaternary climate change. Earth-Science Reviews 207, 103220.
Gee, G.W. and Or, D. (2002) 2.4 Particle-Size Analysis, Methods of Soil Analysis, pp. 255-293.
George, B.G., Maitra, A. and Anczkiewicz, R. (2024) Monsoon control on evolution of the western Indian aeolian landscape: Insights from U-Pb detrital zircon geochronology and Sr-Nd-Hf isotope studies of the Thar Desert sand dunes. Geomorphology, 109429.
Gili, S., Gaiero, D.M., Goldstein, S.L., Chemale Jr, F., Koester, E., Jweda, J., Vallelonga, P. and Kaplan, M.R. (2016) Provenance of dust to Antarctica: A lead isotopic perspective. Geophys. Res. Lett. 43, 2291-2298.
Goldstein, S.J. and Jacobsen, S.B. (1987) The Nd and Sr isotopic systematics of river-water dissolved material: Implications for the sources of Nd and Sr in seawater. Chemical Geology: Isotope Geoscience section 66, 245-272.
Goswami, V., Singh, S.K., Bhushan, R. and Rai, V.K. (2012) Temporal variations in $^{87}Sr/^{86}Sr$ and ε_{Nd} in sediments of the southeastern Arabian Sea: Impact of monsoon and surface water circulation. Geochem. Geophys. Geosyst. 13, Q01001.
Grousset, F.E. and Biscaye, P.E. (2005) Tracing dust sources and transport patterns using Sr, Nd and Pb isotopes. Chem. Geol. 222, 149-167.
GSI (2020) District Resource Map, Raigad District, Maharashtra, Second ed.
Guinoiseau, D., Singh, S.P., Galer, S.J.G., Abouchami, W., Bhattacharyya, R., Kandler, K., Bristow, C. and Andreae, M.O. (2022) Characterization of Saharan and Sahelian dust sources based on geochemical and radiogenic isotope signatures. Quaternary Science Reviews 293, 107729.
Harlavan, Y., Erel, Y. and Blum, J.D. (1998) Systematic Changes in Lead Isotopic Composition with Soil Age in Glacial Granitic Terrains. Geochimica et Cosmochimica Acta 62, 33-46.
Horbe, A.M.C., Albuquerque, M.F.D.S. and Dantas, E.L. (2022) Nd and Sr Isotopes and REE Investigation in Tropical Weathering Profiles of Amazon Region. Frontiers in Earth Science 10.
Innocent, C., Michard, A., Malengreau, N., Loubet, M., Noack, Y., Benedetti, M. and Hamelin, B. (1997) Sr isotopic evidence for ion-exchange buffering in tropical laterites from the Paraná, Brazil. Chem. Geol. 136, 219-232.
Jacobsen, S.B. and Wasserburg, G.J. (1980) Sm-Nd isotopic evolution of chondrites. Earth and Planetary Science Letters 50, 139-155.
Jensen, L.S. (1976) A new cation plot for classifying subalkalic volcanic rocks, Ontario Division of Mines Miscellaneous Paper.
Jonell, T.N., Li, Y., Blusztajn, J., Giosan, L. and Clift, P.D. (2018) Signal or noise? Isolating grain size effects on Nd and Sr isotope variability in Indus delta sediment provenance. Chemical Geology 485, 56-73.
Kale, V.S. and Pande, K. (2022) Reappraisal of Duration and Eruptive Rates in Deccan Volcanic Province, India. J. Geol. Soc. India 98, 7-17.
Karri, D., Bikkina, S. and Singh, S.K. (2024) Tracing the provenance of mineral dust over the northern and southern Indian Oceans during the GEOTRACES-India (GI-01, GI-02) expeditions. Geochim. Cosmochim. Acta 366, 141-153.
Kessarkar, P.M., Rao, V.P., Ahmad, S.M. and Babu, G.A. (2003) Clay minerals and Sr–Nd isotopes of the sediments along the western margin of India and their implication for sediment provenance. Marine Geology 202, 55-69.
Krishnamurthy, P. (2020) The Deccan Volcanic Province (DVP), India: A Review. Journal of the Geological Society of India 96, 9-35.

Kulkarni, Y.R., Tripathy, G.R., Sangode, S.J., Naga Kumar, K.C.V., Demudu, G. and Nageswara Rao, K. (2024) Geochemical evidence for increased sediment supply from the Deccan basalts during the Late Holocene aridity. Quat. Int. 707, 24-34.

Kumar, A., Abouchami, W., Galer, S.J.G., Garrison, V.H., Williams, E. and Andreae, M.O. (2014) A radiogenic isotope tracer study of transatlantic dust transport from Africa to the Caribbean. Atmospheric Environment 82, 130-143.

Kumar, A., Abouchami, W., Galer, S.J.G., Singh, S.P., Fomba, K.W., Prospero, J.M. and Andreae, M.O. (2018) Seasonal radiogenic isotopic variability of the African dust outflow to the tropical Atlantic Ocean and across to the Caribbean. Earth and Planetary Science Letters 487, 94-105.

Li, J., Zhang, G., Ruan, L., Yang, J. and Wang, H. (2016) Sr–Nd elements and isotopes as tracers of dust input in a tropical soil chronosequence. Geoderma 262, 227-234.

Li, Y., Clift, P.D., Böning, P., Blusztajn, J., Murray, R.W., Ireland, T., Pahnke, K., Helm, N.C. and Giosan, L. (2018) Continuous Holocene input of river sediment to the Indus Submarine Canyon. Mar. Geol. 406, 159-176.

Lugmair, G.W. and Galer, S.J.G. (1992) Age and isotopic relationships among the angrites Lewis Cliff 86010 and Angra dos Reis. Geochim. Cosmochim. Acta 56, 1673-1694.

Luo, K., Ma, J., Wang, Z., Zhu, G., Zeng, T. and Wei, G. (2024) Fractionation Mechanism and Flux Estimation of Strontium Isotopes During Basalt Weathering. Geochemistry, Geophysics, Geosystems 25, e2023GC011215.

Ma, J., Wei, G., Xu, Y. and Long, W. (2010) Variations of Sr–Nd–Hf isotopic systematics in basalt during intensive weathering. Chemical Geology 269, 376-385.

Mason, T.F.D., Widdowson, M., Ellam, R.M. and Oxburgh, R. (2000) Isotopic variability of Sr and Nd in lateritic deposits from the Deccan Traps, India: evidence for an input of aeolian material to the laterites, J. Conf. Abstr, pp. 674-675.

McLennan, S.M. (1993) Weathering and global denudation. The Journal of Geology 101, 295-303.

McLennan, S.M. (2001) Relationships between the trace element composition of sedimentary rocks and upper continental crust. Geochemistry, Geophysics, Geosystems 2.

Melluso, L. and Sethna, S.F. (2011) Mineral Compositions in the Deccan Igneous Rocks of India: An Overview, in: Ray, J., Sen, G., Ghosh, B. (Eds.), Topics in Igneous Petrology. Springer Netherlands, Dordrecht, pp. 135-159.

Meyer, I., Davies, G.R. and Stuut, J.-B.W. (2011) Grain size control on Sr-Nd isotope provenance studies and impact on paleoclimate reconstructions: An example from deep-sea sediments offshore NW Africa. Geochemistry, Geophysics, Geosystems 12.

Millot, R., Allègre, C.-J., Gaillardet, J. and Roy, S. (2004) Lead isotopic systematics of major river sediments: a new estimate of the Pb isotopic composition of the Upper Continental Crust. Chemical Geology 203, 75-90.

Mitra, A., Sen, I.S., Pandey, S.K., Velu, V., Reisberg, L., Bizimis, M., Cloquet, C. and Nizam, S. (2021) Lead Isotope Evidence for Enhanced Anthropogenic Particle Transport to the Himalayas during Summer Months. Environmental Science & Technology 55, 13697-13708.

Nauret, F., Famin, V., Vlastélic, I. and Gannoun, A. (2019) A trace of recycled continental crust in the Réunion hotspot. Chemical Geology 524, 67-76.

Nesbitt, H.W., Markovics, G. and price, R.C. (1980) Chemical processes affecting alkalis and alkaline earths during continental weathering. Geochim. Cosmochim. Acta 44, 1659-1666.

Nesbitt, H.W. and Young, G.M. (1982) Early Proterozoic climates and plate motions inferred from major element chemistry of lutites. Nature 299, 715-717.

Nesbitt, H.W. and Young, G.M. (1984) Prediction of some weathering trends of plutonic and volcanic rocks based on thermodynamic and kinetic considerations. Geochim. Cosmochim. Acta 48, 1523-1534.

Öhlander, B., Ingri, J., Land, M. and Schöberg, H. (2000) Change of Sm-Nd isotope composition during weathering of till. Geochim. Cosmochim. Acta 64, 813-820.

Ollier, C.D. and Sheth, H.C. (2008) The High Deccan duricrusts of India and their significance for the 'laterite' issue. J. Earth Syst. Sci. 117, 537-551.

Peketi, A., Mazumdar, A., Pillutla, S.P.K., Sawant, B. and Gupta, H. (2021) Climatic and Tectonic Control on the Bengal Fan Sedimentation Since the Pliocene. 22, e2020GC009448.

Peng, Z.X., Mahoney, J., Hooper, P., Harris, C. and Beane, J. (1994) A role for lower continental crust in flood basalt genesis? Isotopic and incompatible element study of the lower six formations of the western Deccan Traps. Geochimica et Cosmochimica Acta 58, 267-288.

Pryor, E.J., Hall, I.R., Simon, M.H., Andersen, M., Babin, D., Starr, A., Lipp, A. and van der Lubbe, H.J.L. (2025) Geochemical—Mineralogical Constraints on the Provenance of Sediment Supplied From South African River Catchments Draining Into the Southwestern Indian Ocean. Geochemistry, Geophysics, Geosystems 26, e2024GC011869.

Qasim, A., Singh, S.P., Ahmad, N., Argal, J. and Chandrashekhar, A.K. (2022) Inter-estuarine and seasonal to decadal variations of heavy metal pollution in the Gulf of Cambay, India. Environmental Monitoring and Assessment 194, 36.

Rahaman, W., Chanakya, I.V.S., Ray, I., Tarique, M., Fousiya, A.A., Das, R. and Misra, S. (2024) Anthropogenic Lead (Pb) deposition history of the western Indian Ocean from coral-based Pb/Ca ratio and Pb isotope records. Science of The Total Environment 955, 177312.

Rahaman, W., Singh, S.K., Sinha, R. and Tandon, S.K. (2009) Climate control on erosion distribution over the Himalaya during the past ~100 ka. Geology 37, 559-562.

Sahu, S., Singh, S.P., Qasim, A., Ahmad, N. and Bhattacharyya, R. (2025) Terrane Specific REE Composition in the Bulk Materials of Modern Soils and Aquatic Sediments as a Reliable Provenance Tracer in a Progressive Weathering Scenario. Available at SSRN 5385399.

Schoene, B., Eddy, M.P., Samperton, K.M., Keller, C.B., Keller, G., Adatte, T. and Khadri, S.F.R. (2019) U-Pb constraints on pulsed eruption of the Deccan Traps across the end-Cretaceous mass extinction. Science 363, 862-866.

Sen, I.S., Bizimis, M., Tripathi, S.N. and Paul, D. (2016) Lead isotopic fingerprinting of aerosols to characterize the sources of atmospheric lead in an industrial city of India. Atmospheric Environment 129, 27-33.

Sharma, A.K., Dalai, T.K., Kisku, P.C., Pattanaik, J.K., Misra, S., Verma, S. and Shukla, A.D. (2025) Release and partitioning of neodymium and its radiogenic isotope during basaltic weathering. Chemical Geology 692, 122957.

Shukla, A., Singh, S.K., Singh, D.P., Sharma, A. and Dimri, A.P. (2024) Strong Climate Control on the Millennial-Scale Dust Variability and Sediment

Provenances in the Equatorial Indian Ocean Inferred From Sr-Nd Isotopes. Paleoceanography and Paleoclimatology 39, e2023PA004808.

Singh, A., Thomsen, K.J., Sinha, R., Buylaert, J.-P., Carter, A., Mark, D.F., Mason, P.J., Densmore, A.L., Murray, A.S., Jain, M., Paul, D. and Gupta, S. (2017) Counter-intuitive influence of Himalayan river morphodynamics on Indus Civilisation urban settlements. Nature Communications 8, 1617.

Singh, S.K., Rai, S.K. and Krishnaswami, S. (2008) Sr and Nd isotopes in river sediments from the Ganga Basin: Sediment provenance and spatial variability in physical erosion. Journal of Geophysical Research: Earth Surface 113.

Singh, U., Suresh, K., Prabhat, P., Rahaman, W. and Kumar, A. (2023) Geochemical tracing of synoptic scale modern dust transport over the Northeast Arabian Sea during the southwest monsoon. Sci. Tot. Environ. 893, 164438.

Su, N., Wu, Z., Yang, S. and Xu, J. (2022) Re-assessing the effect of differential weathering of minerals on strontium stable isotope behavior during granodiorite weathering. Chemical Geology 613, 121160.

Suresh, K., Singh, U., Kumar, A., Karri, D., Peketi, A. and Ramaswamy, V. (2021) Provenance tracing of long-range transported dust over the Northeastern Arabian Sea during the southwest monsoon. Atmospheric Research 250, 105377.

Vaasma, T.J.E.J.o.E. (2008) Grain-size analysis of lacustrine sediments: a comparison of pre-treatment methods. 57.

Weis, D., Kieffer, B., Maerschalk, C., Barling, J., de Jong, J., Williams, G.A., Hanano, D., Pretorius, W., Mattielli, N., Scoates, J.S., Goolaerts, A., Friedman, R.M. and Mahoney, J.B. (2006) High-precision isotopic characterization of USGS reference materials by TIMS and MC-ICP-MS. Geochem. Geophys. Geosyst. 7, 1-30.

White, W.M., Albarède, F. and Télouk, P. (2000) High-precision analysis of Pb isotope ratios by multi-collector ICP-MS. Chemical Geology 167, 257-270.

Whitehouse, M.J. (1990) Isotopic evolution of the southern Outer Hrebridean Lewisian gneiss complex: Constraints on late Archaean source regions and the generation of transposed Pb-PbPb□Pb palaeoisochrons. Chemical Geology: Isotope Geoscience section 86, 1-20.

Widdowson, M. and Cox, K.G. (1996) Uplift and erosional history of the Deccan Traps, India: Evidence from laterites and drainage patterns of the Western Ghats and Konkan Coast. Earth and Planetary Science Letters 137, 57-69.

Widdowson, M. and Gunnell, Y. (1995) Lateritization, Geomorphology and Geodynamics of a Passive Continental Margin: The Konkan and Kanara Coastal Lowlands of Western Peninsular India, Palaeoweathering, Palaeosurfaces and Related Continental Deposits, pp. 245-274.

Yadav, C., Singh, S.K. and Chinni, V. (2025) Persistent elevated levels of dissolved lead in the Indian Ocean post-leaded gasoline ban: The impact of anthropogenic activities, sediment desorption, and dust storms. Mar. Pollut. Bull. 215, 117874.

Yu, Z., Colin, C., Wan, S., Saraswat, R., Song, L., Xu, Z., Clift, P., Lu, H., Lyle, M., Kulhanek, D., Hahn, A., Tiwari, M., Mishra, R., Miska, S. and Kumar, A. (2019) Sea level-controlled sediment transport to the eastern Arabian Sea over the past 600 kyr: Clay minerals and SrNd isotopic evidence from IODP site U1457. Quaternary Science Reviews 205, 22-34.

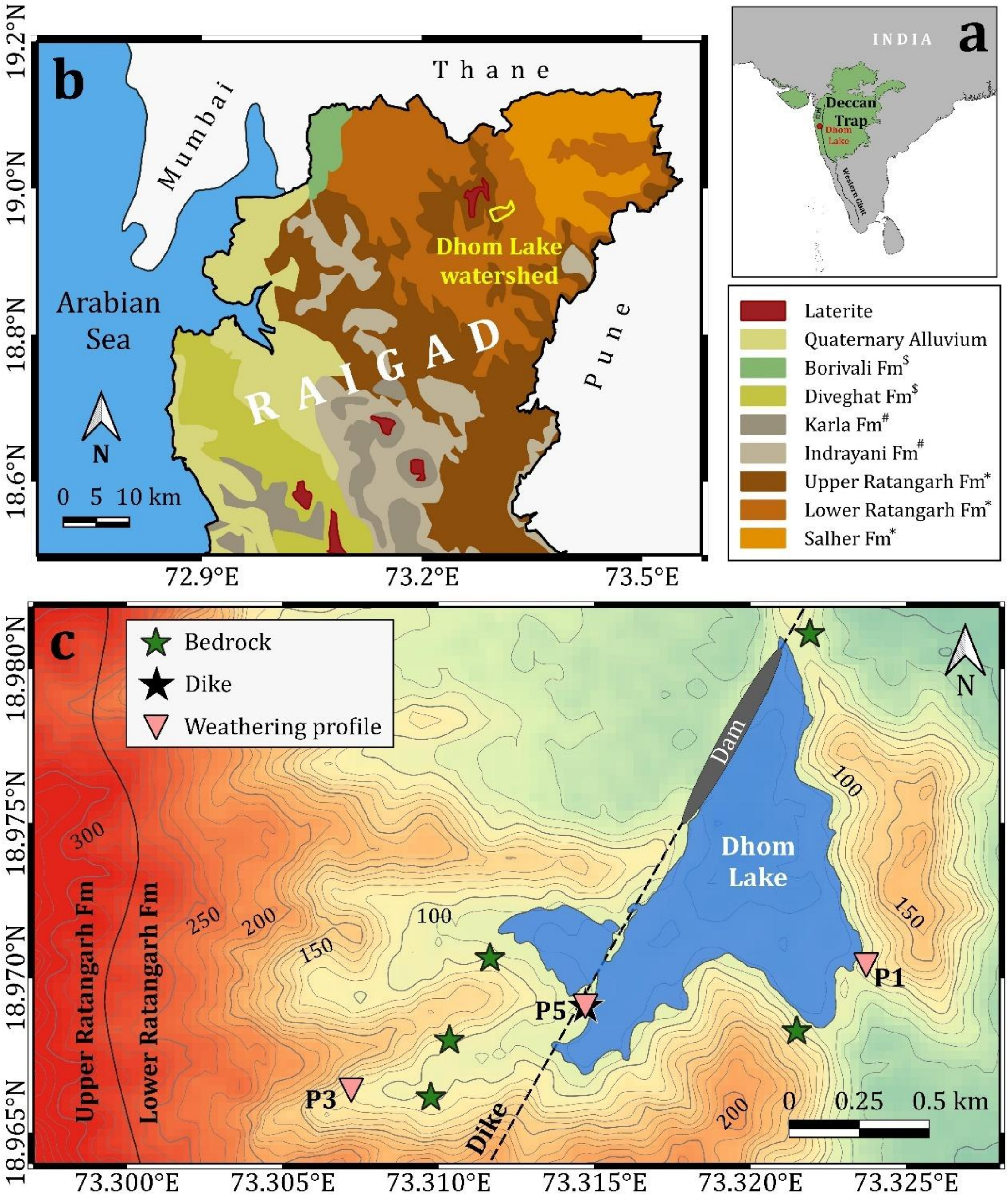

Fig. 1: (a) The Deccan Trap aerial extent and the locations of the Western Ghat, Konkan Coastal Belt (KCB), and Dhom Lake watershed marked in the map of India, (b) the watershed overlain on the lithological map (GSI, 2020) of the northern Raigad (Maharashtra), and (c) the locations of the bedrock/dike outcrops and weathering profiles sampled from the watershed are shown. Fig. 1b legend superscripts refer to different lava formations belonging to the [*]Kalsubai, [#]Lonavala, and [$]Wai subgroups. The elevation contours in Fig. 1c are extracted using a Digital Elevation Model (DEM) image retrieved from the Shuttle Radar Topography Mission (SRTM). The Upper Ratangarh–Lower Ratangarh formation boundary and a dike exposed at the lake periphery are also shown.

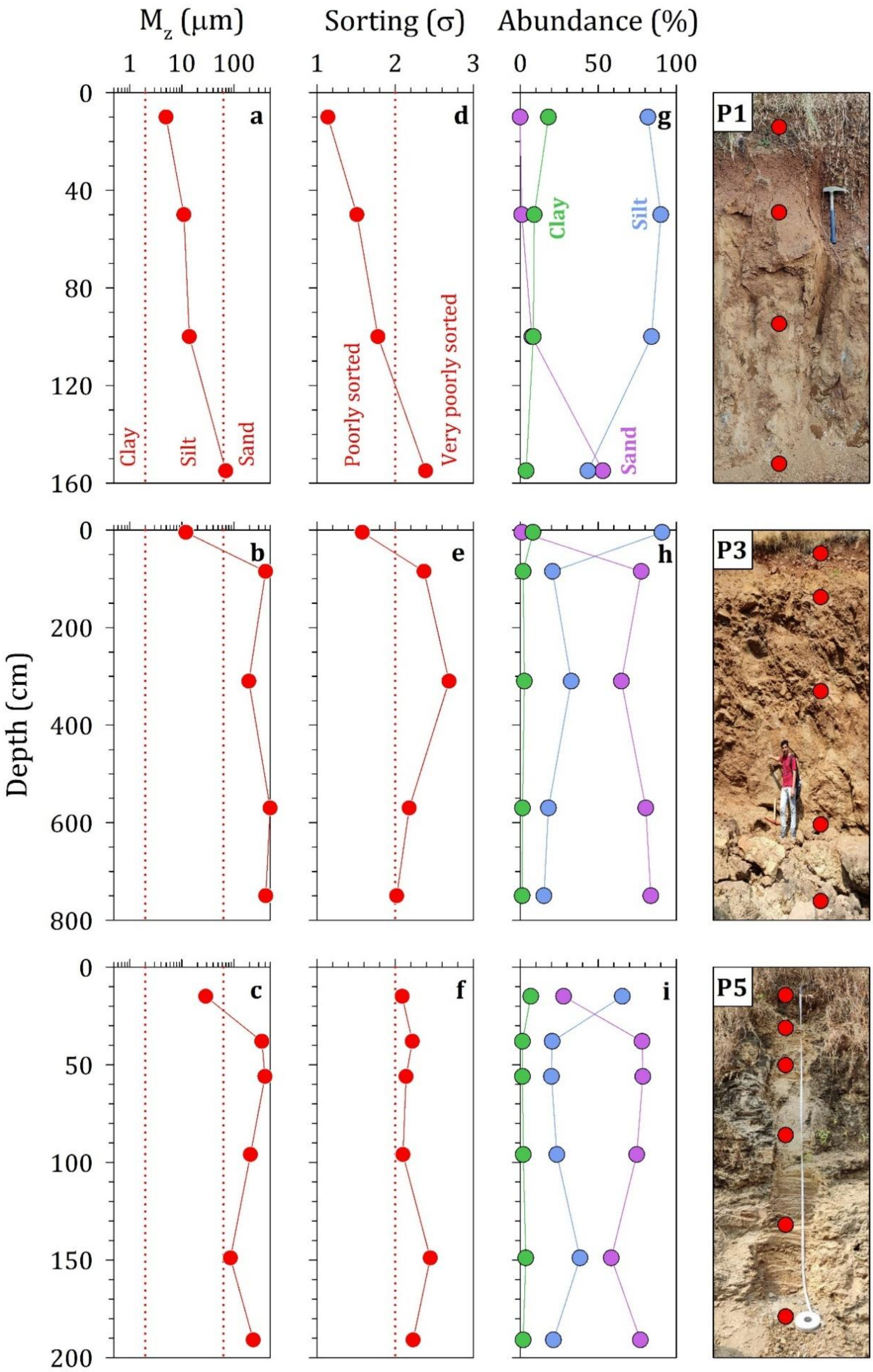

Fig. 2: The vertical distributions of (a–c) mean grain size (M_z), (d–f) sorting (σ), (g–i) relative sand-silt-clay abundances in the bulk materials of weathering profiles (P1, P3, and P5). The sampling heights of these profiles are indicated in the field photographs, shown in the rightmost panel.

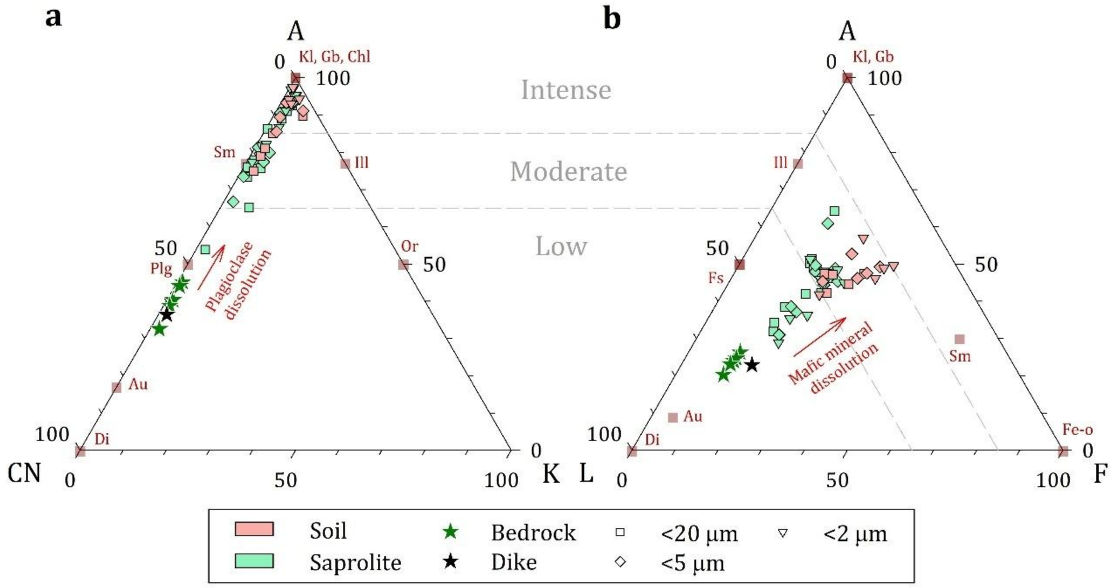

Fig. 3: The ternary plots of (a) Al_2O_3–(CaO^*+Na_2O)–K_2O (A–CN–K diagram; Nesbitt and Young, 1982) and (b) Al_2O_3–(Na_2O+K_2O+MgO+CaO^*)–Fe_2O_3 (A–L–F diagram; Babechuk et al., 2014) for the soil/saprolite FLF, and the bedrock/dike samples. The compositions of kaolinite (Kl), gibbsite (Gb), chlorite (Chl), smectite (Sm), plagioclase (Plg), augite (Au), diopside (Di), illite (Ill), orthoclase (Or), feldspar (Fs), and iron oxide (Fe-o) minerals are also shown.

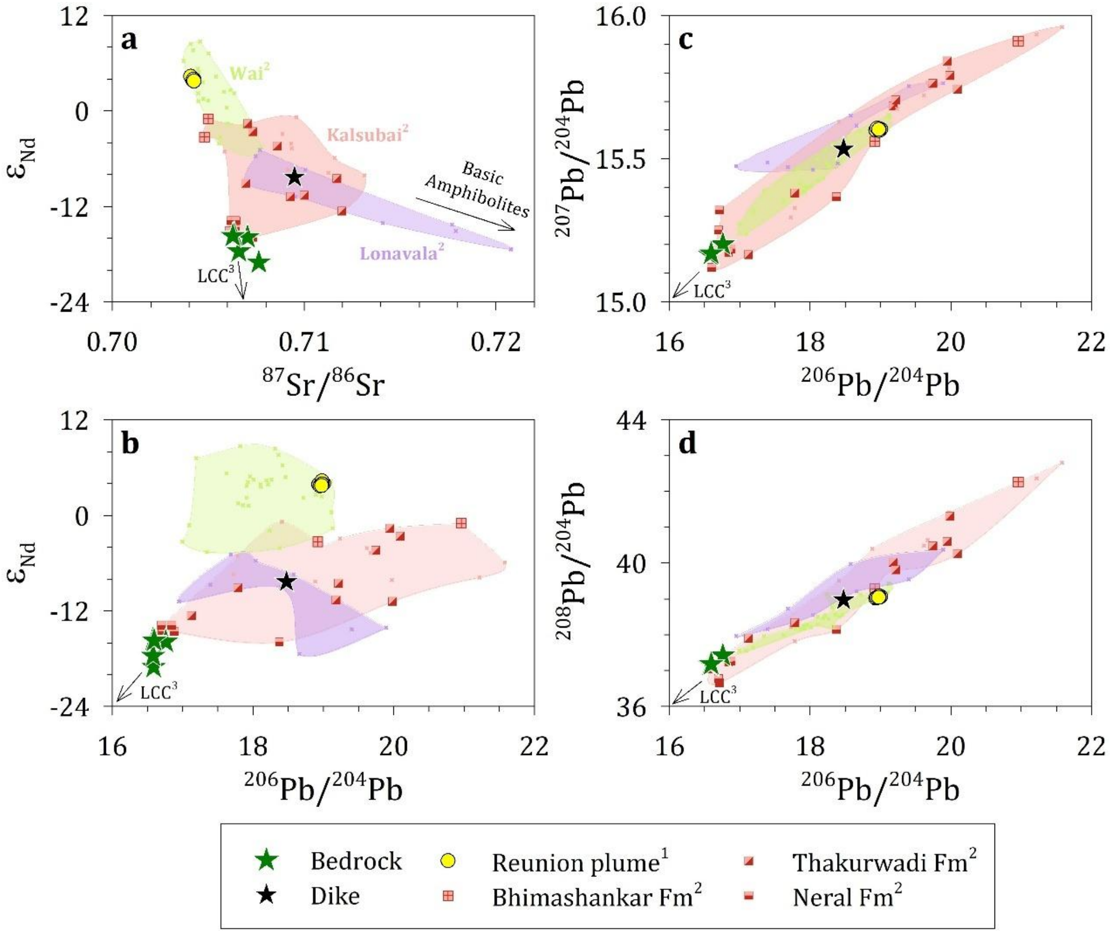

Fig. 4: The scatter plots of (a) $^{87}Sr/^{86}Sr$–ε_{Nd}, (b) $^{206}Pb/^{204}Pb$–ε_{Nd}, (c) $^{206}Pb/^{204}Pb$–$^{207}Pb/^{204}Pb$, and (d) $^{206}Pb/^{204}Pb$–$^{208}Pb/^{204}Pb$ for the bedrock and dike samples. Data Source: [1]Nauret et al. (2019), [2]Basu et al. (2020), and [3]Whitehouse (1990).

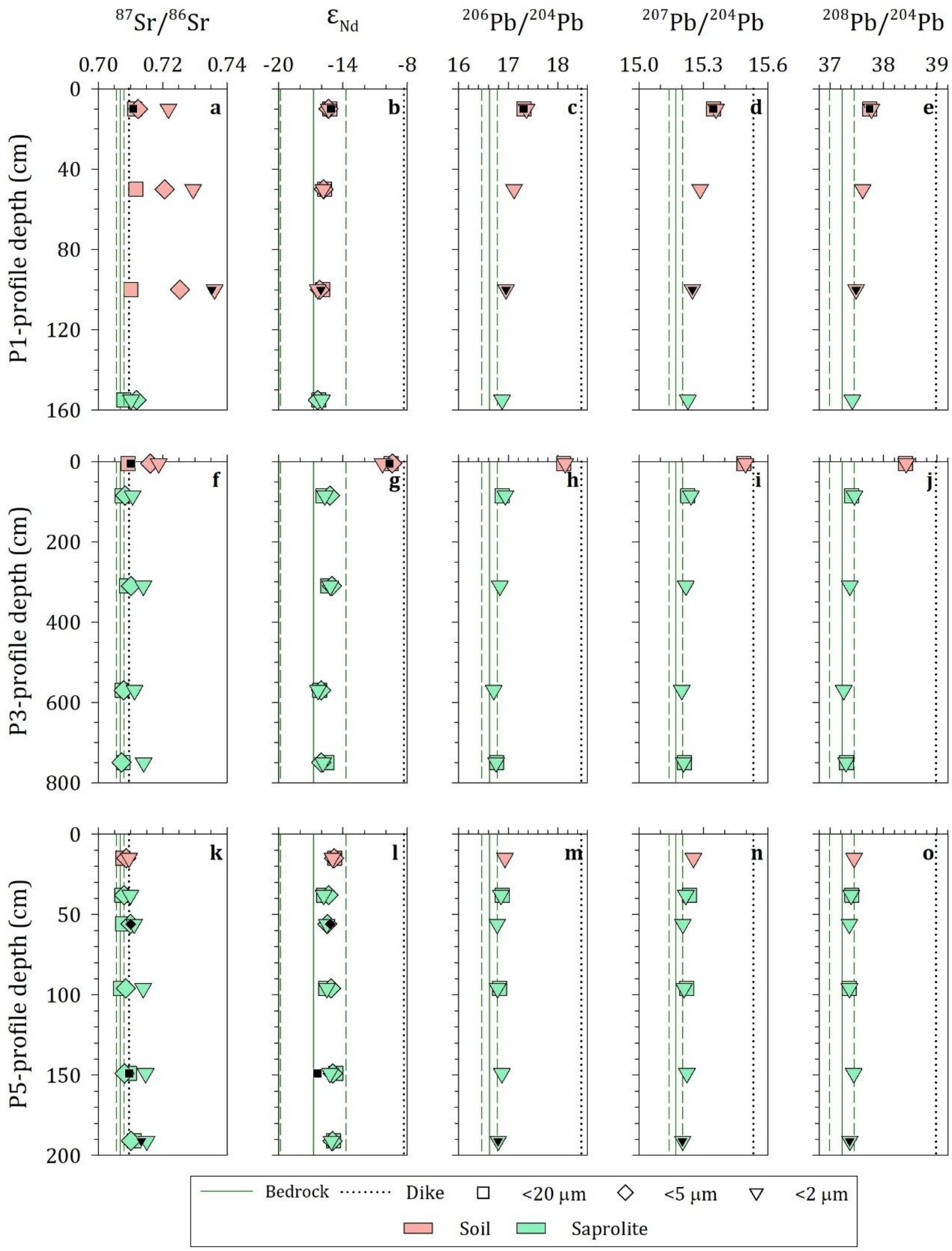

Fig. 5: The vertical distributions of $^{87}Sr/^{86}Sr$, ε_{Nd}, $^{206}Pb/^{204}Pb$, $^{207}Pb/^{204}Pb$, and $^{208}Pb/^{204}Pb$ in the soil/saprolite for (a–e) P1 profile, (f–j) P3 profile, and (k–o) P5 profile. Please note that the filled black symbols are the duplicate samples of the respective grain-size fraction. The vertical green and black lines refer to the bedrock (mean ± 2 SD; solid and short dashed) and dike (dotted) compositions, respectively.

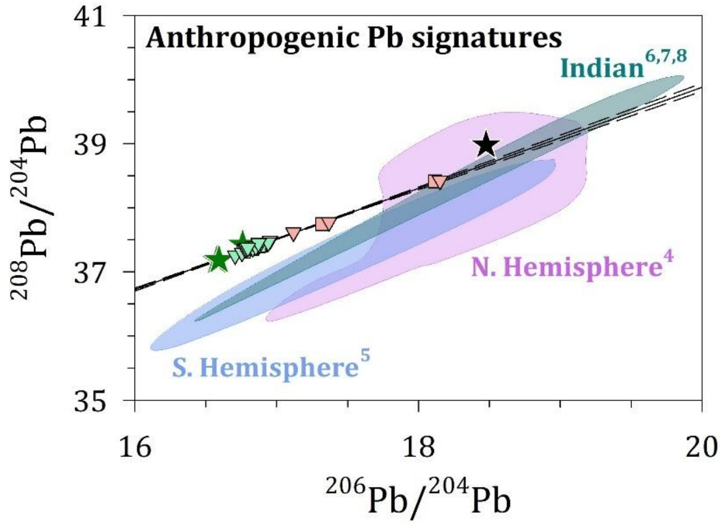

Fig. 6: The scatter plot of $^{206}Pb/^{204}Pb$–$^{208}Pb/^{204}Pb$ of the bedrock/dike samples and soil/saprolite FLF samples. The regression lines (solid and dashed, CI 95 %) of the soil/saprolite FLF are also shown. The colored areas enclose the global and Indian anthropogenic Pb compositions. Data Source: [4]Bollhöfer and Rosman (2001), [5]Bollhöfer and Rosman (2000), [6]Sen et al. (2016), [7]Mitra et al. (2021), and [8]Das et al. (2018).

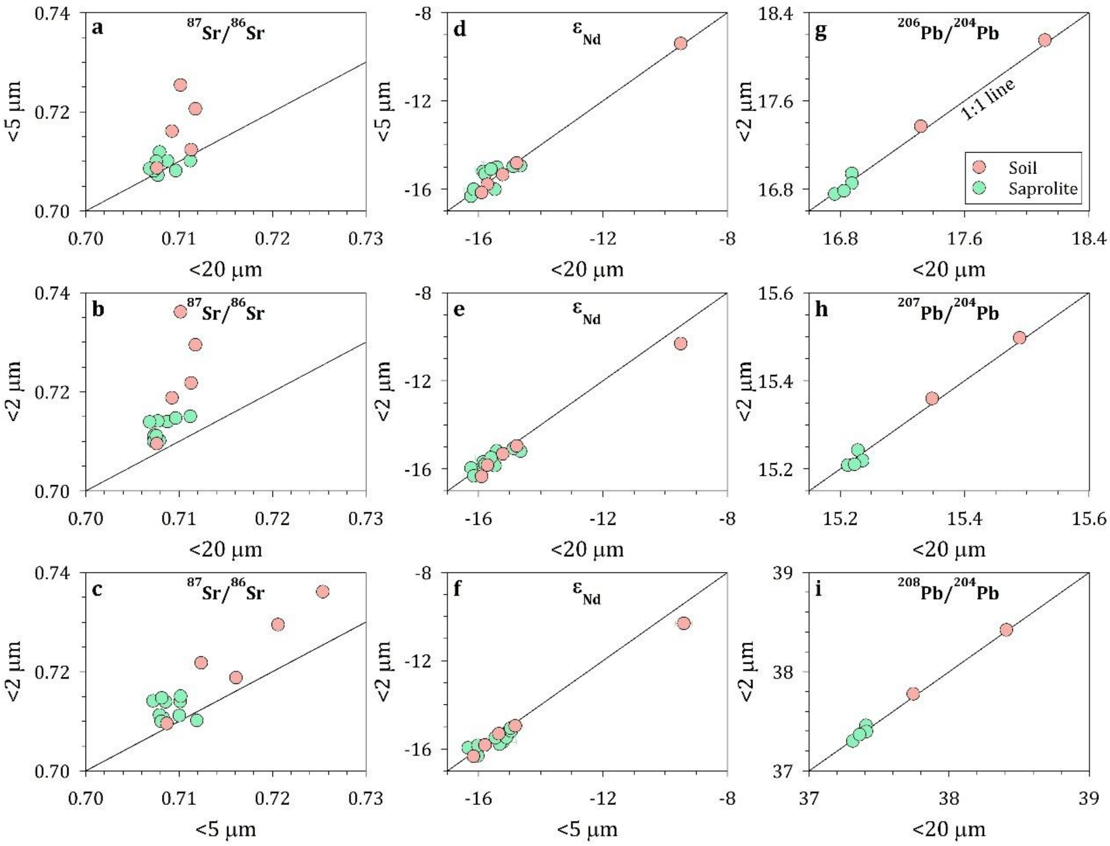

Fig. 7: The cross plots of Sr, Nd, and Pb isotope compositions in different grain-sized soil/saprolite FLF.

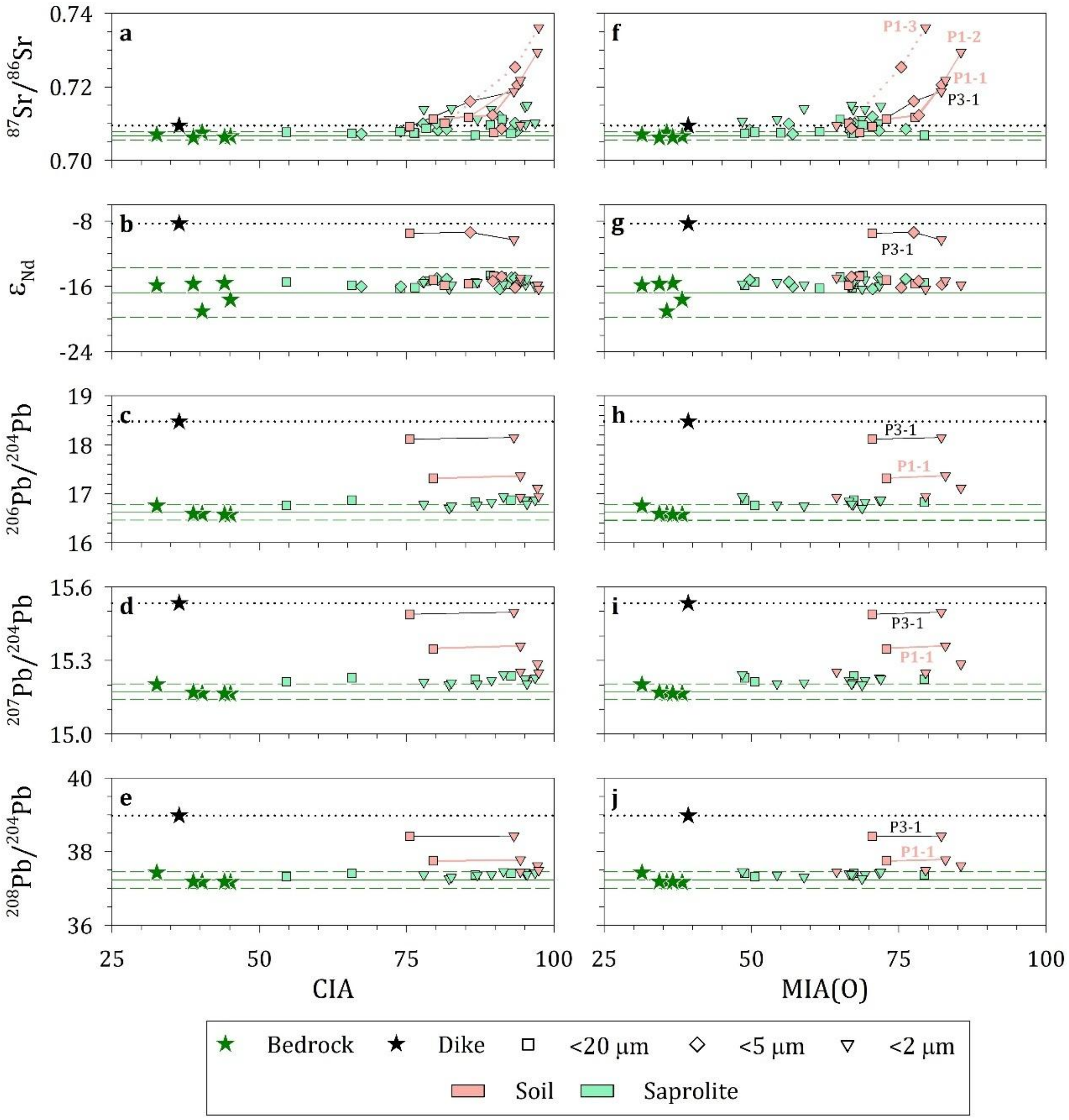

Fig. 8: The scatter plots of CIA (a–e) and MIA(O) (f–j) versus $^{87}Sr/^{86}Sr$, ε_{Nd}, $^{206}Pb/^{204}Pb$, $^{207}Pb/^{204}Pb$, and $^{208}Pb/^{204}Pb$ for the bedrock/dike and different grain-sized soil/saprolite FLF. The horizontal green and black lines refer to the bedrock (mean ± 2 SD; solid and short dashed) and dike (dotted) compositions, respectively.

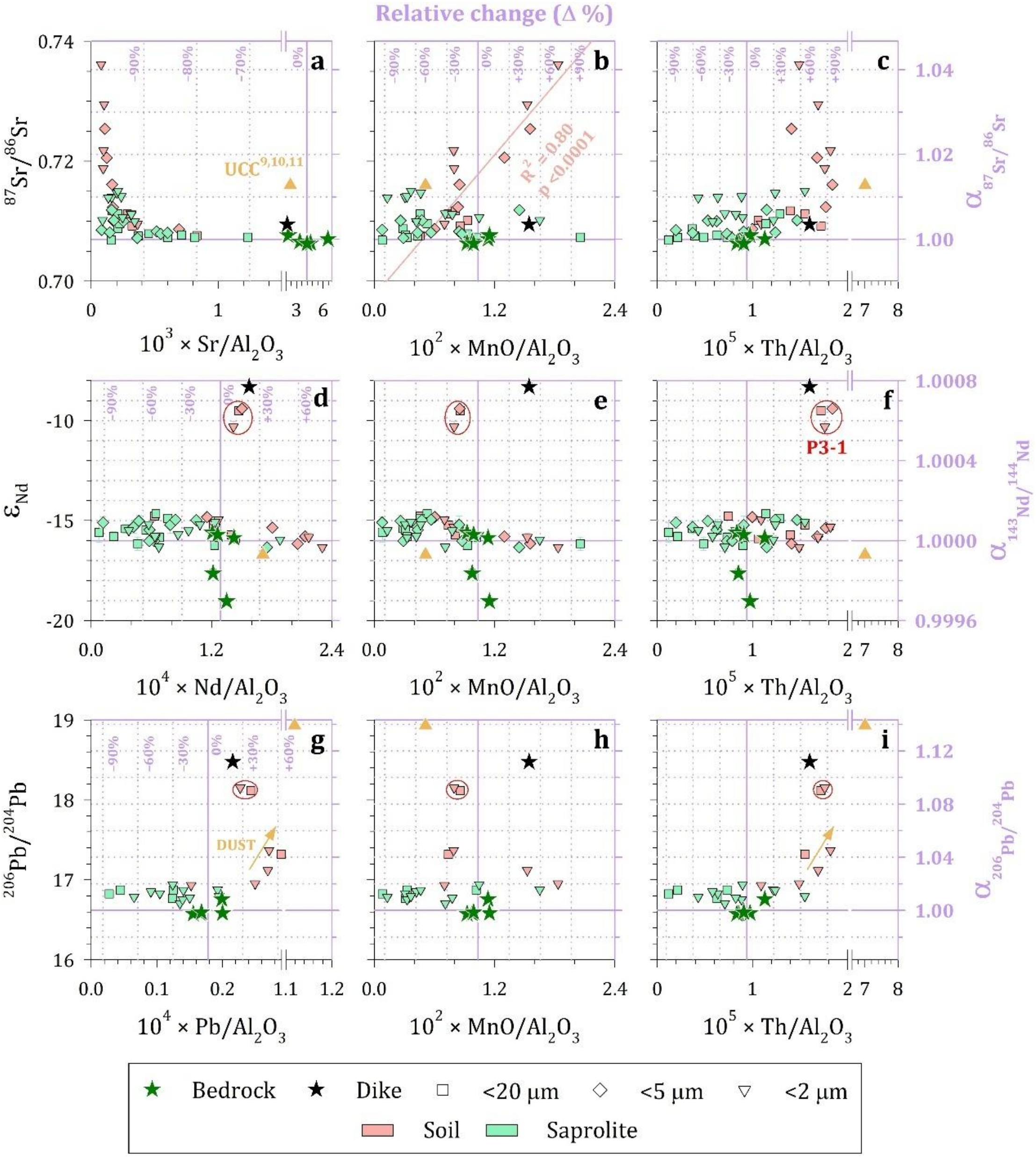

Fig. 9: The scatter plots of (a) Sr/Al_2O_3–$^{87}Sr/^{86}Sr$, (b) MnO/Al_2O_3–$^{87}Sr/^{86}Sr$, (c) Th/Al_2O_3–$^{87}Sr/^{86}Sr$, (d) Nd/Al_2O_3–ε_{Nd}, (e) MnO/Al_2O_3–ε_{Nd}, (f) Th/Al_2O_3–ε_{Nd}, (g) Pb/Al_2O_3–$^{206}Pb/^{204}Pb$, (h) MnO/Al_2O_3–$^{206}Pb/^{204}Pb$, and (i) Th/Al_2O_3–$^{206}Pb/^{204}Pb$ of the bedrock/dike and soil/saprolite FLF. The UCC composition is adapted from [9]Millot et al. (2004), [10]Goldstein and Jacobsen (1987), and [11]McLennan (2001). This figure also includes the additional scales of the bedrock-normalized relative change in elemental abundances and radiogenic isotope fractionation factors (α, which is equal to the isotopic ratio of the sample divided by the same isotopic ratio of the bedrock).

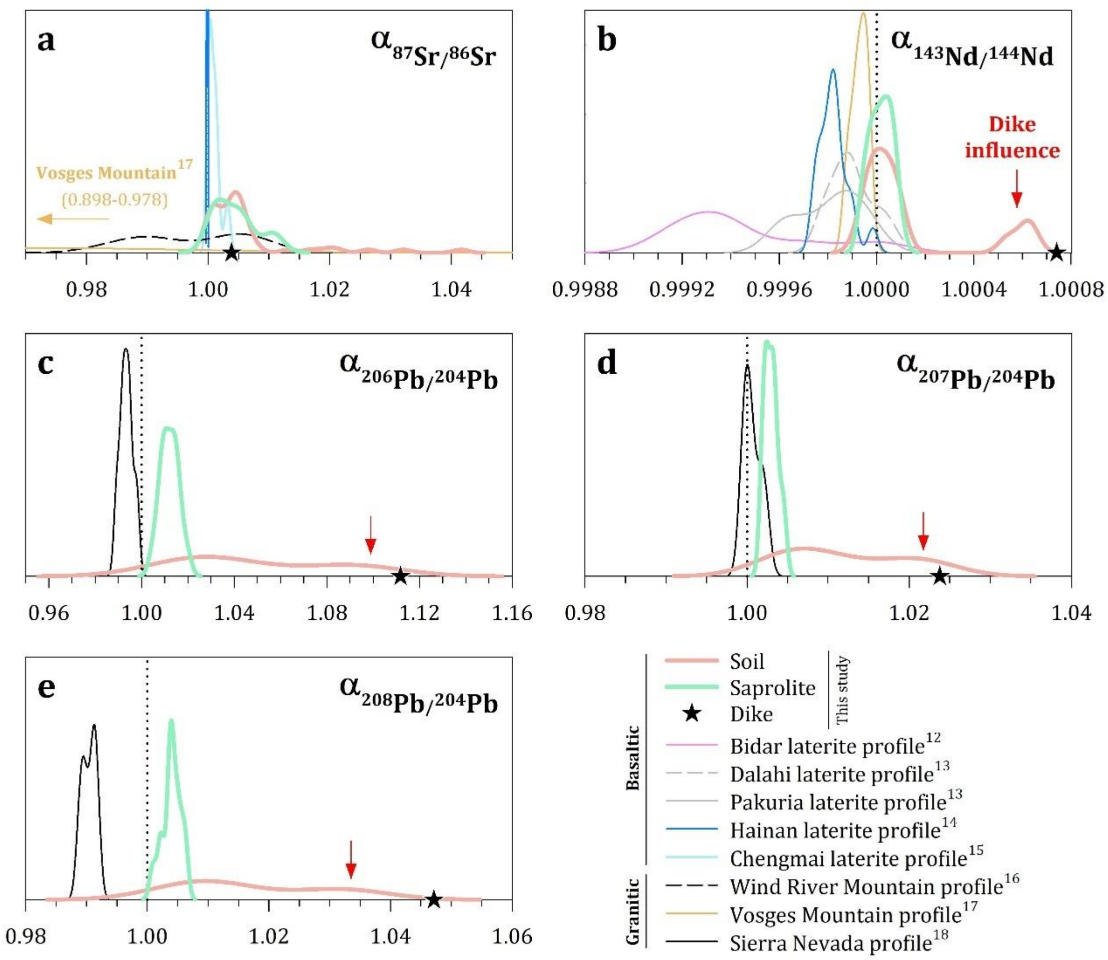

Fig. 10: Probability distribution of (a) $\alpha_{87Sr/86Sr}$, (b) $\alpha_{143Nd/144Nd}$, (c) $\alpha_{206Pb/204Pb}$, (d) $\alpha_{207Pb/204Pb}$, and (e) $\alpha_{208Pb/204Pb}$ for the soil/saprolite FLF (this study) and the weathering profiles from the literature. The literature data used here are from [12]Babechuk et al. (2015), [13]Sharma et al. (2025), [14]Ma et al. (2010), [15]Luo et al. (2024), [16]Blum and Erel (1997), [17]Aubert et al. (2001), and [18]Harlavan et al. (1998).

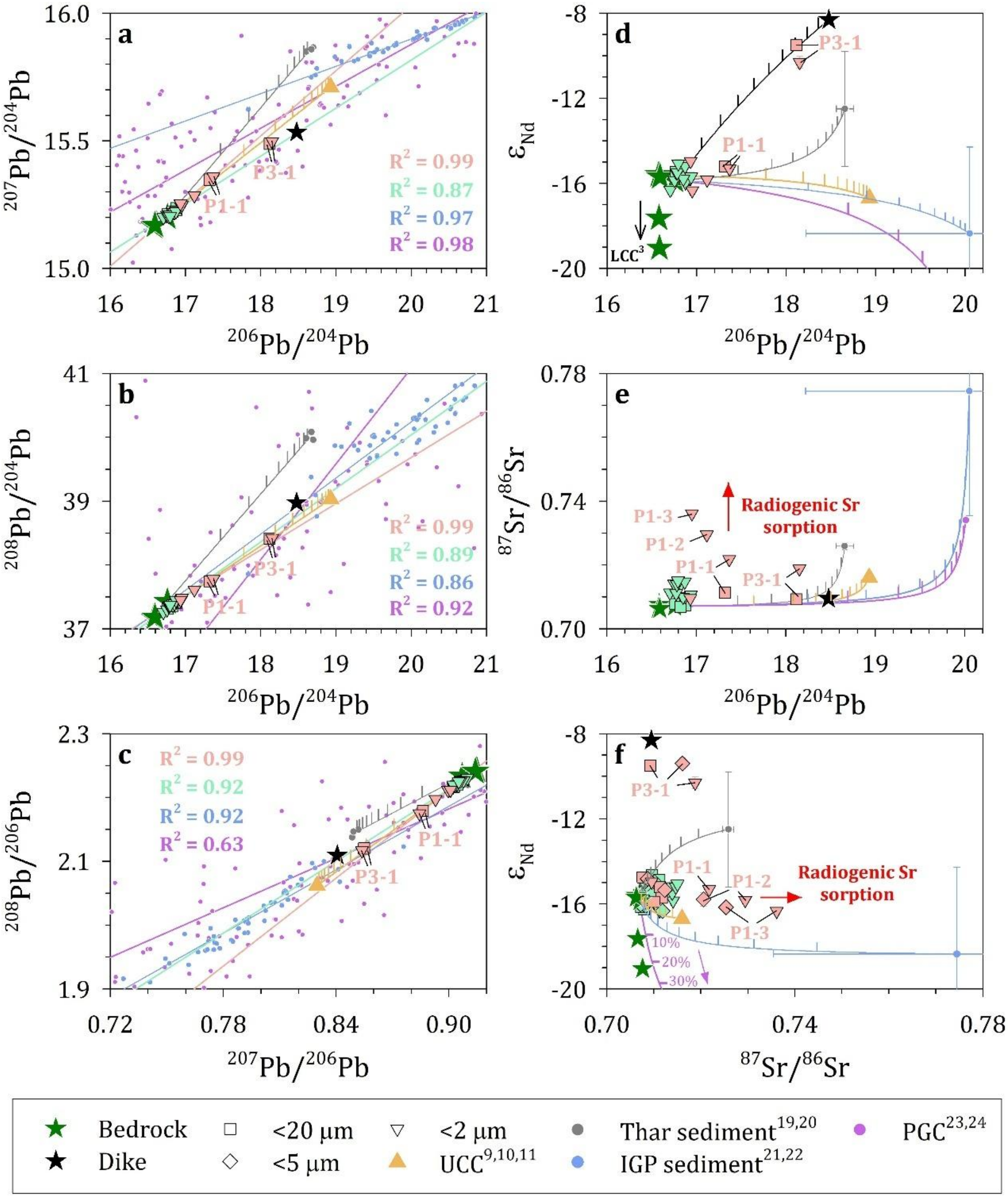

Fig. 11: The scatter plots of (a) $^{206}Pb/^{204}Pb$–$^{207}Pb/^{204}Pb$, (b) $^{206}Pb/^{204}Pb$–$^{208}Pb/^{204}Pb$, (c) $^{207}Pb/^{206}Pb$–$^{208}Pb/^{206}Pb$, (d) $^{206}Pb/^{204}Pb$–ε_{Nd}, (e) $^{206}Pb/^{204}Pb$–$^{87}Sr/^{86}Sr$, and (f) $^{87}Sr/^{86}Sr$–ε_{Nd} of different grain-sized soil/saprolite FLF and the bedrock/dike samples. The endmember mixing proportions at 10 % increment levels are also shown. The literature data used here are from [9]Millot et al. (2004), [10]Goldstein and Jacobsen (1987), [11]McLennan (2001), [19]Bhattacharyya et al. (2024), [20]Ferrat et al. (2012), [21]Singh et al. (2008), [22]Garçon and Chauvel (2014), [23]Shukla et al. (2024), and [24]Digis (2024).

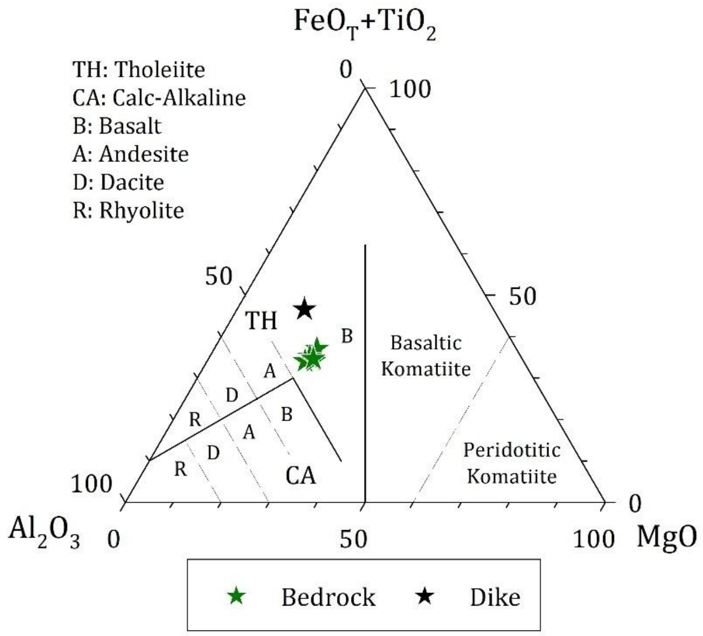

Fig. S1: The ternary diagram of (FeO$_T$+TiO$_2$)–Al$_2$O$_3$–MgO (Jensen, 1976) for the volcanic rock classification of the bedrock and dike samples.